

The report is based on studies performed at Lincoln Laboratory, a contract research center, by Massachusetts Institute of Technology. It was prepared for the Department of the Air Force under Contract F-9648-93-C-0000.

This report may be reproduced to satisfy needs of U.S. Government agencies.

The ESC/Pratic Affairs Office has reviewed this report and has recommended that it be placed in the National Technical Information Service, where it will be available to the general public, including foreign nationals.

This technical report has been reviewed and is approved for distribution.

ROBERT S. COVYMAN, DFR


Gary J. Klinger
Administrative Controlling Officer
Contract Support Management

Non-Confidential

PLEASE DO NOT RETURN

Permission is given to destroy this document
when it is no longer needed.

**MASSACHUSETTS INSTITUTE OF TECHNOLOGY
LINCOLN LABORATORY**

SOLID STATE RESEARCH

QUARTERLY TECHNICAL REPORT

1 NOVEMBER 1994 — 31 JANUARY 1995

ISSUED 10 AUGUST 1995

Approved for public release; distribution is unlimited.

LEXINGTON

MASSACHUSETTS

ABSTRACT

This report covers in detail the research work of the Solid State Division at Lincoln Laboratory for the period 1 November 1994 through 31 January 1995. The topics covered are Electrooptical Devices, Quantum Electronics, Materials Research, Submicrometer Technology, High Speed Electronics, Microelectronics, and Analog Device Technology. Funding is provided primarily by the Air Force, with additional support provided by the Army, ARPA, Navy, BMDO, NASA, and NIST.

TABLE OF CONTENTS

Abstract		iii
List of Illustrations		vii
List of Tables		ix
Introduction		xi
Reports on Solid State Research		xiii
Organization		xix
1.	ELECTROOPTICAL DEVICES	1
1.1	Improved Tapered-Gain-Region Lasers at 1.3 μm with Output Powers > 1 W	1
1.2	Smart-Pixel Arrays for Early Vision	3
2.	QUANTUM ELECTRONICS	7
2.1	Ultraviolet Generation with Passively <i>Q</i> -Switched Picosecond Microchip Lasers	7
3.	MATERIALS RESEARCH	11
3.1	Growth of GaSb from Triethylgallium and Trisdimethylaminoantimony	11
3.2	Tritertiarybutylaluminum As a New Organometallic Source for Epitaxial Growth of AlGaSb	15
4.	SUBMICROMETER TECHNOLOGY	21
4.1	Nitrogen-Arrival-Rate-Limited Growth of GaN Using an Electron-Cyclotron-Resonance Discharge Source in Gas-Source Molecular Beam Epitaxy	21
4.2	Color Separation Echelon Gratings	26
5.	HIGH SPEED ELECTRONICS	33
5.1	Self-Aligned GaAs MISFETs with a Low-Temperature-Grown GaAs Gate Insulator	33
6.	MICROELECTRONICS	37
6.1	Packaging of a 1960 \times 2560-Pixel Charge-Coupled Device Imager	37
7.	ANALOG DEVICE TECHNOLOGY	41
7.1	Lincoln/Hughes Compressive Receiver Demonstration with 24-ns Bonded-Wafer $\text{YBa}_2\text{Cu}_3\text{O}_{7-\delta}$ Chirp Filters	41

LIST OF ILLUSTRATIONS

Figure No.		Page
1-1	Device design of tapered laser for 1.3- μm operation. The ridge waveguide and tapered region lengths are 1 and 2 mm, respectively. The output aperture width is 210 μm .	1
1-2	CW output power vs current for 1.3- μm tapered laser with ridge waveguide section.	2
1-3	Far-field beam profile at 1 W for 1.3- μm tapered-gain-region laser. The power in the central diffraction lobe is 85% of total.	2
1-4	First stage of artificial retina implemented using smart-pixel arrays and microlenses.	4
1-5	Monolithic optoelectronic transistor (MOET) with dual optical inputs. The optical output is a function of the ratio of the power levels of the optical inputs.	5
1-6	Transfer characteristic of MOET. The abscissa is the logarithm of the ratio of the powers of the two optical inputs I_{left} and I_{right} , and the ordinate is the modulator photocurrent, which is proportional to $1-R$, where R is the modulator reflectivity.	5
2-1	Frequency-quadrupled passively Q -switched picosecond microchip laser.	7
2-2	Time-averaged output of packaged frequency-quadrupled passively Q -switched picosecond microchip laser at fundamental wavelength (1.064 μm), second harmonic (532 nm), and fourth harmonic (266 nm) as a function of temperature.	8
3-1	Surface morphology of GaSb layer grown with TEGa and TDMA S b; $T = 575^\circ\text{C}$ and $V/\text{III} = 1$.	12
3-2	Fourier transform infrared absorption spectra of TDMA S b and TEGa; TDMA S b; and TEGa.	13
3-3	Minimum V/III ratio for stoichiometric growth of GaSb grown with TDMA S b and TEGa.	13
3-4	Double crystal x-ray diffraction curve of GaSb grown on GaSb substrate by TEGa and TDMA S b, and TEGa and TMSb.	14
3-5	Low-temperature photoluminescence spectrum of GaSb.	14
3-6	Surface morphology of $\text{Al}_x\text{Ga}_{1-x}\text{Sb}$ layer grown at $T = 550^\circ\text{C}$.	16

LIST OF ILLUSTRATIONS (Continued)

Figure No.		Page
3-7	Dependence of AlSb incorporation on TTBAI vapor phase composition where x_{vapor} is the ratio of the TTBAI mole fraction to the total group III (TTBAI and TEGa) mole fraction.	17
3-8	Variation of (a) hole concentration and (b) hole mobility at 77 K with AlSb composition.	18
3-9	Hole mobility vs concentration for $\text{Al}_x\text{Ga}_{1-x}\text{Sb}$ grown by organometallic vapor phase epitaxy.	19
3-10	Low-temperature photoluminescence spectra of $\text{Al}_x\text{Ga}_{1-x}\text{Sb}$.	19
4-1	Ion spectrum as measured by quadrupole mass analyzer with ionizer filament current off: (a) Spectrum showing ions at 14 amu (N^+ or N_2^{++}) and 28 amu (N_2^+) peaks; (b) same spectrum as in (a) but magnified 250 times, showing 7 amu (N^{++}), 20 amu (Ne^+), 40 amu (Ar^+), and 42 amu (N_3^+), as well as 14 and 28 amu peaks. The horizontal scan covers a mass-to-charge ratio of 0 to 50 amu. The N_2 mass flow is 3.3 sccm, and the RF net power is 20 W.	22
4-2	Ion current as function of N_2 mass flow for ion species indicated in Figure 4-1. The electron-cyclotron-resonance (ECR) RF net power is 20 W.	23
4-3	Normalized 14- and 28-amu ion currents and GaN growth rate, plotted as function of N_2 mass flow. The ECR RF net power is 20 W.	24
4-4	GaN growth rate as function of gallium flux and N_2 mass flow, normalized to GaN (0001) plane monolayer (ML) gallium density. For convenience, the growth rate is expressed in both $\text{\AA}/\text{h}$ and ML/s. Indicated on the figure is the line where the Ga flux equals the GaN growth rate. All data below 800 $\text{\AA}/\text{h}$ are at a net RF power of 20 W.	25
4-5	Survey of undoped GaN electron mobilities as function of carrier concentrations from Molnar et al. [5] and references therein. Also included are the present Lincoln results at RF powers of 20 W (dashed line) and 38 and 60 W (single data points). The solid line is drawn to aid the eye.	25
4-6	20-keV Reflection electron diffraction pattern from GaN along the $[2\bar{1}\bar{1}0]$ direction grown on (0001) sapphire. The substrate temperature is 950°C, and the nitrogen plasma beam is on.	26
4-7	Color separation by dispersion in (a) conventional stepped grating and (b) binary optics echelon grating.	27

LIST OF ILLUSTRATIONS (Continued)

Figure No.		Page
4-8	Schematic diagram showing two lithographic steps required to fabricate a binary optics component with four phase levels. This sequence can be generalized to fabricate 2^M phase levels using M lithographic steps.	28
4-9	Predicted spectral efficiency as function of wavelength for both scalar diffraction theory model and rigorous electromagnetic (EM) calculations. The -1 , 0 , and $+1$ order efficiencies are plotted as a function of wavelength.	29
4-10	Grating performance showing white light transmitted (a) through microlens array and (b) through color separation grating and microlens array.	30
5-1	Layer structures and process steps for self-aligned LTG GaAs MISFET: (a) Deposition of W gate, (b) etching off LTG GaAs and AlAs layers, (c) self-aligned n^+ implantation, and (d) deposition and alloying of ohmic contacts.	34
5-2	I_{ds} vs V_{ds} characteristics of MISFETs with $100\text{-}\mu\text{m}$ -wide gate width. (a) Control MISFET; the vertical scale is 1 mA/div and V_{gs} is $+2\text{ V}$ for the top curve with 1-V steps. (b) Self-aligned MISFET with 30-keV implant; the vertical scale is 2 mA/div and V_{gs} is $+4\text{ V}$ for the top curve with 2-V steps. The horizontal scale is 500 mV/div for all the I-V curves.	35
6-1	Photographs of (a) front and (b) back of packaged large-area charge-coupled device imager.	38
6-2	Schematic of electrostatic discharge circuit that protects each clock line.	40
7-1	Illustration of LaAlO_3 wafer bonding technique used to fabricate 24-ns stripline YBCO chirp filters. The 24-ns filter is shown as an inset.	42
7-2	Group delay vs frequency characteristic measured using downchirp ports of 24-ns YBCO chirp filter.	43
7-3	Time-domain response of 24-ns YBCO chirp filter: (a) Time-domain reflectometry measured at 77 K for one of the two YBCO striplines that constitute the 24-ns filter and (b) low-frequency time-domain response to a step function measured at 77 K .	43
7-4	System block diagram for Lincoln/Hughes demonstration. Interfaces to the Hughes receiver and computer system are indicated.	44

LIST OF TABLES

Table No.		Page
6-1	Comparison Between Coefficient of Thermal Expansion of Silicon and Other Materials	39
7-1	Summary of Lincoln/Hughes Compressive Receiver Demonstration	45

INTRODUCTION

1. ELECTROOPTICAL DEVICES

Improved InP-based tapered lasers for operation at $\lambda = 1.3 \mu\text{m}$ have demonstrated continuous output power $> 1 \text{ W}$. The far-field patterns have 85% of the output power in a central diffraction-limited lobe.

In an approach to image preprocessing using smart-pixel arrays, a modified version of the monolithic optoelectronic transistor has been designed that responds to local image contrasts. The epitaxial structure for this smart-pixel circuit has been grown and the circuit components fabricated and characterized; simulations have shown that the circuit responds to contrast ratios and is robust to variations in absolute illumination levels.

2. QUANTUM ELECTRONICS

A fiber-pumped passively Q -switched Nd:YAG microchip laser has been frequency quadrupled to produce $0.5\text{-}\mu\text{J}$ ultraviolet pulses of 250-ps duration at repetition rates up to 13 kHz. The entire device is contained in a 3-cm-long \times 1-cm-diam package.

3. MATERIALS RESEARCH

GaSb epilayers have been grown by organometallic vapor phase epitaxy (OMVPE) using triethylgallium (TEGa) and a new Sb source, trisdimethylaminoantimony (TDMASb), which has a thermal decomposition temperature lower than that of the conventional Sb source, trimethylantimony, and therefore is more efficient for growth at low temperature ($< 600^\circ\text{C}$). However, prereactions between TEGa and TDMASb sources, which were observed by Fourier transform infrared spectroscopy, resulted in a degraded surface morphology.

A new organometallic source, tritertiarybutylaluminum, has been used for the first time in the growth of $\text{Al}_x\text{Ga}_{1-x}\text{Sb}$ by low-pressure OMVPE, and alloys grown over the whole composition range $0 < x \leq 1$ exhibited mirror surface morphologies. Photoluminescence was observed for all layers with $x < 0.2$ (the composition range where the energy bandgap is direct), and all layers were p -type with hole concentrations increasing with x and saturating at about $4 \times 10^{18} \text{ cm}^{-3}$ for $x = 1$.

4. SUBMICROMETER TECHNOLOGY

Growth of GaN at high substrate temperatures has been demonstrated under conditions of nitrogen-arrival-rate-limited growth. These conditions significantly reduce the residual n -type conductivity of GaN usually attributed to nitrogen vacancies.

An echelon grating structure has been fabricated for use in a color projection display. The grating efficiently separates the incident white light into red, blue, and green diffractive orders.

5. HIGH SPEED ELECTRONICS

GaAs MISFETs with a low-temperature-grown (LTG) GaAs gate insulator and ion-implanted self-aligned source and drain n^+ regions have been demonstrated in which, because of the reduced source and drain resistance, the drain saturation current and the transconductance increased more than twofold compared to regular MISFETs. The LTG GaAs insulator, which maintains its high resistivity and breakdown strength after the implantation and 800°C activation annealing, keeps a very low gate leakage current.

6. MICROELECTRONICS

A new packaging method has been developed for a 1960×2560 -pixel wafer-scale charge-coupled device imager. The package offers substantial advantages over conventional approaches in maintaining low noise, having a good thermal expansion match to silicon, and offering opportunities to place circuitry close to the device.

7. ANALOG DEVICE TECHNOLOGY

The dispersive delay of a 2-GHz-bandwidth, high-temperature superconductive (HTS) chirp filter has been increased to 24 ns using a new thinner stripline structure. This HTS chirp filter has been employed to double the instantaneous bandwidth coverage of a modern Hughes electronic-warfare compressive receiver to 2 GHz, compared to the traditionally used surface-acoustic-wave chirp filter.

REPORTS ON SOLID STATE RESEARCH

1 NOVEMBER 1994 THROUGH 31 JANUARY 1995

PUBLICATIONS

- | | | |
|--|--|--|
| Linearized Modulator for Sub-Octave-Bandpass Optical Analog Links | G. E. Betts | <i>IEEE Trans. Microwave Theory Tech.</i> 42 , 2642 (1994) |
| Radiative Renormalization Applied to Strong Field, Resonant Nonlinear Optical Interactions | O. Blum*
T. K. Gustafson*
P. L. Kelley | In <i>Nonlinear Optics and Optical Physics</i> , I. C. Khoo, J. F. Lam, and F. Simoni, eds. (World Scientific, River Edge, N.J., 1994) |
| A New Face-Centered-Cubic Photonic Crystal for Microwave and Millimeter-Wave Applications | E. R. Brown
K. Agi*
C. Dill III
C. D. Parker
K. J. Malloy* | <i>Microw. Opt. Technol. Lett.</i> 7 , 777 (1994) |
| An Orthogonal-Transfer CCD Imager | B. E. Burke
R. K. Reich
E. D. Savoye
J. L. Tonry* | <i>IEEE Trans. Electron Devices</i> 41 , 2482 (1994) |
| 3.9- μm InAsSb/AlAsSb Double-Heterostructure Diode Lasers with High Output Power and Improved Temperature Characteristics | H. K. Choi
G. W. Turner
Z. L. Liau | <i>Appl. Phys. Lett.</i> 65 , 2251 (1994) |

*Author not at Lincoln Laboratory.

Mosaic Diamond Substrates Approaching Single-Crystal Quality Using Cube-Shaped Diamond Seeds	M. W. Geis N. N. Efremow R. Susalka J. C. Twichell K. A. Snail* C. Spiro* B. Sweeting* S. Holly*	<i>Diamond Related Mater.</i> 4, 76 (1994)
Strained-Layer InGaAsP Diode Lasers with Tapered Gain Region for Operation at $\lambda = 1.3 \mu\text{m}$	S. H. Groves J. P. Donnelly J. N. Walpole J. D. Woodhouse L. J. Missaggia R. J. Bailey A. Napoleone	<i>IEEE Photon. Technol. Lett.</i> 6, 1286 (1994)
High-Efficiency, High-Temperature Mid-Infrared ($\lambda \geq 4 \mu\text{m}$) InAsSb/GaSb Lasers	H. Q. Le G. W. Turner J. R. Ochoa A. Sanchez	<i>Electron. Lett.</i> 30, 1944 (1994)
Measurement and Model for Correlating Phase and Baseband 1/f Noise in an FET	R. D. Martinez* D. E. Oates R. C. Compton*	<i>IEEE Trans. Microwave Theory Tech.</i> 42, 2051 (1994)
Q-Switched Operation of Quasi-Three-Level Lasers	C. D. Nabors	<i>IEEE J. Quantum Electron.</i> 30, 2896 (1994)
MIT Program to Demonstrate Superconductive Components in Microwave Systems	R. W. Ralston	<i>Proceedings of 43rd International Wire and Cable Symposium (IWCS, Eatontown, N.J., 1994), p. 150</i>

*Author not at Lincoln Laboratory.

ACCEPTED FOR PUBLICATION

High-Performance AlGaAs/GaAsP Tensile-Strained Quantum-Well Laser Diodes	F. Agahi* K. M. Lau* H. K. Choi A. Baliga* N. G. Anderson*	<i>IEEE Photon. Technol. Lett.</i>
High-Power, High-Temperature Operation of GaInAsSb-AlGaAsSb Ridge-Waveguide Lasers Emitting at 1.9 μm	H. K. Choi G. W. Turner M. K. Connors S. Fox* C. Dauga* M. Dagenais*	<i>IEEE Photon. Technol. Lett.</i>
CH ₃ I Vapor Etching of Masked and Patterned GaAs	C. W. Krueger C. A. Wang D. Hsieh* M. Flytzani- Stephanopoulos*	<i>J. Cryst. Growth</i>
Coupled-Cavity Electro-Optically Q-Switched Nd:YVO ₄ Microchip Lasers	J. J. Zayhowski C. Dill III	<i>Opt. Lett.</i>

PRESENTATIONS[†]

Device Applications and Characterization of GaAs Grown at Low Temperatures by Molecular Beam Epitaxy	R. A. Murphy	Lincoln Laboratory Technical Seminar Series, University of Illinois, Urbana, Illinois, 2 November 1994
Low-Power Adaptive Filter	A. M. Chiang	1994 Government Microcircuit Applications Conference, San Diego, California, 7-10 November 1994

*Author not at Lincoln Laboratory.

[†]Titles of presentations are listed for information only. No copies are available for distribution.

Microwave Vortex Dynamics as a Function of Frequency and Temperature in the Random Pinning Potential of $\text{YBa}_2\text{Cu}_3\text{O}_7$	N. R. Belk D. E. Oates G. Dresselhaus* M. S. Dresselhaus*	1994 Fall Meeting of the Materials Research Society, Boston, Massachusetts, 28 November–2 December 1994
Microwave Power Dependence of $\text{YBa}_2\text{Cu}_3\text{O}_{7-x}$ Thin Film Josephson Edge Junctions	P. P. Nguyen* D. E. Oates G. Dresselhaus* G. Koren* E. Polturaki*	
Photolithography at 193 nm	M. Rothschild	Semiconductor Equipment and Materials International Technology Symposium 1994, Makuhari Messe-Chiba, Japan, 30 November–2 December 1994
Resonant-Tunneling-Diode Circuits	T. C. L. G. Sollner E. R. Brown C-L. Chen C. G. Fonstad* W. D. Goodhue R. H. Mathews J. P. Sage	Advanced Heterostructure Workshop, Kohala Coast, Hawaii, 4-9 December 1994
Diamond Field-Emission Cathodes	M. W. Geis J. C. Twichell M. B. Stern N. N. Efremow K. E. Krohn T. M. Lyszczarz R. Uttaro	Technical Seminar, Phillips Laboratory, Hanscom Air Force Base, Massachusetts, 21 December 1994
Overview of GaSb-Based Materials Research at MIT Lincoln Laboratory	G. W. Turner H. K. Choi H. Q. Le	25th Winter Colloquim on Quantum Electronics, Snowbird, Utah, 3-6 January 1995

*Author not at Lincoln Laboratory.

Device Applications Issues for High- T_c Passive Microwave Circuits	W. G. Lyons	International Union of Radio Scientists Meeting, Boulder, Colorado, 3-7 January 1995
GaSb-Based Mid-Infrared Semiconductor Lasers	H. K. Choi G. W. Turner H. Q. Le	International Conference on Narrow Gap Semiconductors, Santa Fe, New Mexico, 9-12 January 1995
High-Power Diode-Laser-Pumped Mid-Infrared HgCdTe/CdZnTe Quantum Well Lasers	H. Q. Le A. Sanchez J. M. Arias M. Zandian* R. R. Zucca* Y.-Z. Liu*	
Optical Interconnects for Computer Data Communication	D. Z. Tsang	Meeting of the Boston Chapter, IEEE Lasers and Electro-Optics Society, Waltham, Massachusetts, 12 January 1995
Optical Interconnects for Digital Systems	D. Z. Tsang	
Sub-Octave-Bandwidth Analog Link Using Linearized Reflective Modulators	G. E. Betts	5th Annual DARPA Symposium on Photonics Systems for Antenna Applications, Monterey, California, 17-20 January 1995
Diamond Field-Emission Cathodes	M. W. Geis J. C. Twichell M. B. Stern N. N. Efremov K. E. Krohn T. M. Lyszczarz R. Uttaro	Technical Seminar, Westinghouse Science and Technology Center, Pittsburgh, Pennsylvania, 20 January 1995

*Author not at Lincoln Laboratory.

ORGANIZATION

SOLID STATE DIVISION

D. C. Shaver, *Head*
I. Melngailis, *Associate Head*
J. F. Goodwin, *Assistant*
A. L. McWhorter, *Fellow*
D. J. Ehrlich, *Senior Staff*
E. Stern, *Senior Staff*
C. L. Keast, *Staff*
D. Abusch-Magder, *Research Assistant*
T. M. Bloomstein, *Research Assistant*
J. T. Chiou, *Research Assistant*
J. P. Mattia, *Research Assistant*
N. L. DeMeo, Jr., *Associate Staff*
J. W. Caunt, *Assistant Staff*
K. J. Challberg, *Administrative Staff*

SUBMICROMETER TECHNOLOGY

M. Rothschild, *Leader*
T. M. Lyszczarz, *Assistant Leader*
L. H. Dubois, *Senior Staff*[†]

Astolfi, D. K.	Horn, M. W.
Craig, D. M.	Kunz, R. R.
DiNatale, W. F.	Maki, P. A.
Doran, S. P.	Palmateer, S. C.
Efremow, N. N., Jr.	Sedlacek, J. H. C.
Forte, A. R.	Stern, M. B.
Geis, M. W.	Twichell, J. C.
Goodman, R. B.	Uttaro, R. S.
Hartney, M. A.	

QUANTUM ELECTRONICS

A. Sanchez-Rubio, *Leader*
T. Y. Fan, *Assistant Leader*

Aggarwal, R. L.	Jeys, T. H.
Cook, C. C.	Kelley, P. L. [‡]
Daneu, V.	Le, H. Q.
DeFeo, W. E.	Ochoa, J. R.
DiCecca, S.	Zayhowski, J. J.
Dill, C., III	

ELECTRONIC MATERIALS

B-Y. Tsauro, *Leader*
D. L. Spears, *Assistant Leader*

Chen, C. K.	Manfra, M. J.
Choi, H. K.	McGilvary, W. L.
Connors, M. K.	Nitishin, P. M.
Finn, M. C.	Pantano, J. V.
Golovchenko, P. A.	Paul, S. A.*
Harman, T. C.	Reinold, J. H., Jr.
Herrmann, F. P.	Turner, G. W.
Iseler, G. W.	Wang, C. A.
Krohn, L., Jr.	

HIGH SPEED ELECTRONICS

M. A. Hollis, *Leader*
E. R. Brown, *Assistant Leader*
R. A. Murphy, *Senior Staff*

Bozler, C. O.	McIntosh, K. A.
Chen, C. L.	McMahon, O. B.
Goodhue, W. D.	Molnar, R. J.
Harris, C. T.	Nichols, K. B.
Lincoln, G. A., Jr.	Rabe, S.
Mahoney, L. J.	Rathman, D. D.
Mathews, R. H.	

* Research Assistant

† Part Time

‡ Leave of Absence

ELECTROOPTICAL DEVICES

R. C. Williamson, *Leader*
L. M. Johnson, *Assistant Leader*

Aull, B. F.	O'Donnell, F. J.
Bailey, R. J.	Palmacci, S. T.
Betts, G. E.	Poillucci, R. J.
Donnelly, J. P.	Reeder, R. E.
Groves, S. H.	Roussell, H. V.
Hovey, D. L.	Tsang, D. Z.
Liau, Z. L.	Walpole, J. N.
Missaggia, L. J.	Woodhouse, J. D.
Mull, D. E.	

ANALOG DEVICE TECHNOLOGY

R. W. Ralston, *Leader*
T. C. L. G. Sollner, *Assistant Leader*
A. C. Anderson, *Senior Staff*
A. M. Chiang, *Senior Staff*

Arsenault, D. R.	Lyons, W. G.
Boisvert, R. R.	Macedo, E. M., Jr.
Brogan, W. T.	McClure, D. W.
Denneno, J. M.	Murphy, P. G.
Feld, D. A.	Oates, D. E.
Fitch, G. L.	Sage, J. P.
Gleason, E. F.	Seaver, M. M.
Holtham, J. H.	Slattery, R. L.
LaFranchise, J. R.	

MICROELECTRONICS

E. D. Savoye, *Leader*
B. B. Kosicki, *Assistant Leader*
B. E. Burke, *Senior Staff*

Clark, H. R., Jr.	Felton, B. J.	McGonagle, W. H.
Daniels, P. J.	Gregory, J. A.	Mountain, R. W.
Doherty, C. L., Jr.	Hotaling, T. C.	Percival, K. A.
Dolat, V. S.	Johnson, K. F.	Reich, R. K.
Donahue, K. G.	Lind, T. A.	Thomas, J. W. §
Donahue, T. C.	Loomis, A. H.	Young, D. J.

§Staff Associate

1. ELECTROOPTICAL DEVICES

1.1 IMPROVED TAPERED-GAIN-REGION LASERS AT 1.3 μm WITH OUTPUT POWERS > 1 W

For the first tapered-gain-region semiconductor lasers at 1.3- μm wavelength, continuous output powers of 0.5 W were obtained with nearly 80% power in the central lobe of a nearly diffraction-limited far field [1],[2]. Here, we report continuous output powers > 1 W with 85% power in a diffraction-limited central lobe. These advances have resulted from improved fabrication processes and a new device design incorporating a ridge waveguide section with the tapered gain region, a structure reported earlier for 980-nm tapered lasers [3] and similar to that used for a tapered amplifier [4].

The material used for this device has been reported previously. It is a stepped separate-confinement heterostructure with three strained-layer quantum wells, grown by atmospheric-pressure organometallic vapor phase epitaxy. As characterized by broad-area laser results [5], this material has yielded threshold current densities of 176 A/cm² for a 3000- μm cavity length, a transparency current density of 150 A/cm², a peak differential quantum efficiency > 70% for a 250- μm cavity length, and estimated net modal gains of 50 cm⁻¹ at current densities of 1 kA/cm².

The device structure with combined waveguide and tapered gain region is shown in Figure 1-1. A ridge waveguide is used for the single-mode waveguide section, fabricated by dry etching using a CH₄-H₂-Ar plasma. The single-mode ridge section acts as an intracavity mode filter and provides additional gain. A beam propagation model has shown (for the 980-nm lasers) that these features help to ensure good output beam quality [6]. In the devices reported here, the single-mode region was 1 mm long and the tapered region was 2 mm long with an output aperture width of 210 μm .

246467-1

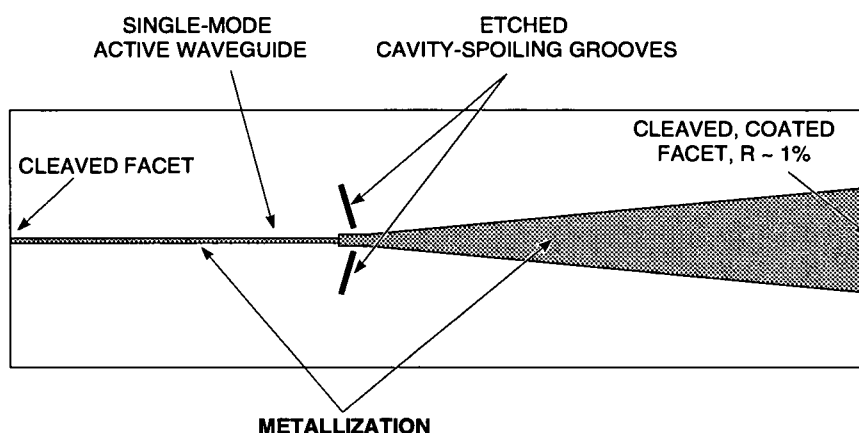


Figure 1-1. Device design of tapered laser for 1.3- μm operation. The ridge waveguide and tapered region lengths are 1 and 2 mm, respectively. The output aperture width is 210 μm .

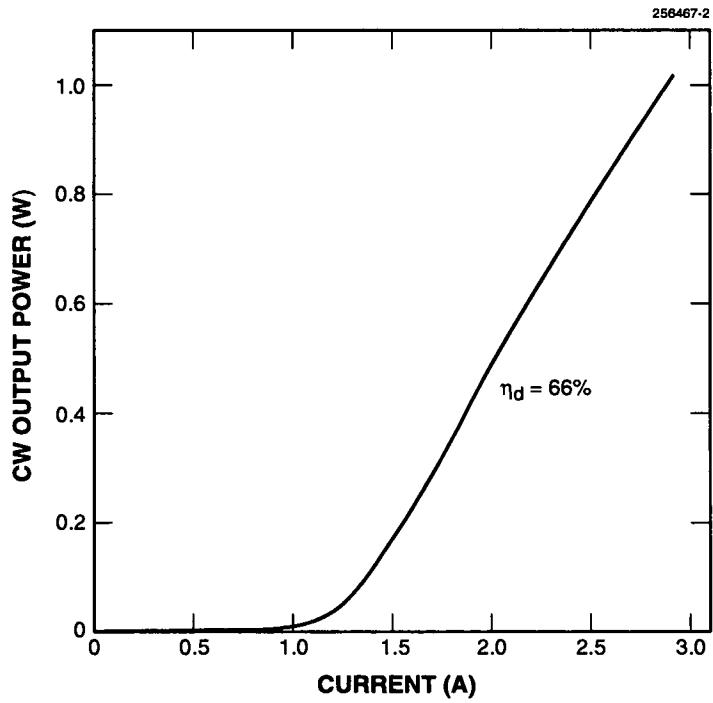


Figure 1-2. CW output power vs current for 1.3- μm tapered laser with ridge waveguide section.

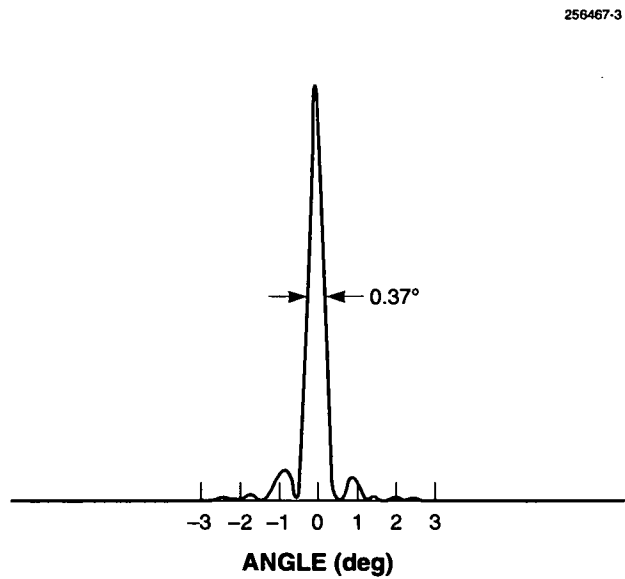


Figure 1-3. Far-field beam profile at 1 W for 1.3- μm tapered-gain-region laser. The power in the central diffraction lobe is 85% of total.

The cw output power vs current is shown in Figure 1-2. Output power exceeding 1 W is achieved. The results also indicate differential quantum efficiencies up to 66%. The far-field beam pattern in the plane of the junction is seen in Figure 1-3. This pattern is obtained by using a lens to remove the phase curvature in that plane resulting from diffraction of the beam as it propagates through the tapered region. About 85% of the output power is in the central lobe of the far-field beam. The angular width of 0.37° is about 1.17 times that of a uniformly illuminated aperture $210 \mu\text{m}$ wide. However, a scan of the optical intensity at the output facet shows that the output aperture is not fully illuminated, which implies that the device output beam is close to diffraction limited. Optimization of the ridge height and width in the single-mode waveguide region in future devices could provide full illumination of the output aperture and, hence, further improvement in output power as a result of better utilization of the tapered gain region by the diffracting beam.

J. N. Walpole J. D. Woodhouse
L. J. Missaggia J. P. Donnelly
S. H. Groves R. J. Bailey
A. Napoleone

1.2 SMART-PIXEL ARRAYS FOR EARLY VISION

The flow of image data through a computer vision system proceeds from preprocessing stages that perform filtering and primitive feature extraction operations to higher-level stages that categorize and draw inferences based on prior knowledge. The preprocessing stages perform computationally intensive data reduction tasks, which are crucial to the success of the higher-level stages. Most preprocessing operations can be implemented with fixed, highly parallel computations. We are developing smart sensors that perform such functions in the analog optical domain using optically interconnected arrays of "smart pixels," i.e., processing circuits with optical inputs and outputs. By performing operations such as center-surround or oriented edge detection in a fully parallel fashion before the image is digitized and passed on to a computer, such smart sensors can greatly reduce the computational overhead associated with preprocessing.

The monolithic optoelectronic transistor (MOET) is a GaAs/AlGaAs smart-pixel circuit that responds in a nonlinear fashion to an optical input signal to produce an optical output. GaAs/AlGaAs multiple-quantum-well diodes are incorporated in the monolithic circuit to detect and modulate surface-normal near-infrared light beams for input and output, respectively. The electrical circuitry provides the nonlinear response and power gain. The first fully integrated MOET was a thresholding device that could switch off a $140\text{-}\mu\text{W}$ output signal in response to a $12.5\text{-}\mu\text{W}$ input signal. Grown by gas-source molecular beam epitaxy, it used a double-barrier resonant tunneling diode to provide the nonlinear response to the input photocurrent and a Schottky-barrier field-effect transistor (FET) to provide amplification [7],[8].

The application of this technology to image sensors with biologically inspired processing features is being investigated. The goal of the effort is to optically cascade two-dimensional arrays of MOETs in

order to perform a series of preprocessing steps on an input image, much in the fashion of the processing layers of the retina and the primary visual cortex. Figure 1-4 shows the first stage of the smart sensor design, which performs a center-surround operation. Each element of the smart-pixel array has a detector pair laid out with doughnut and doughnut-hole geometries. A microlens forms a demagnified image of a region of the input pattern on the associated detector pair. This imaging operation is shown in the figure with solid and dashed arrows, respectively, for two adjacent pixels. Each smart-pixel element produces an optical output that is a function of the contrast between the central portion and the peripheral portion of the corresponding region of the input pattern. The same general scheme can be used to further process the image formed by the optical outputs of the smart-pixel array. A different computation, such as oriented edge detection, is implemented by appropriately modifying the detector geometries [9].

One important feature of biological vision systems is sensitivity to local contrasts rather than to absolute illumination levels or to gradual variations thereof [10],[11]. A new MOET has been designed that responds to local contrast ratios and is robust to absolute illumination levels. Figure 1-5 shows the circuit. Photocurrent from each of the two optical inputs flows through a forward-biased Schottky-barrier diode, thus yielding a voltage that varies logarithmically with the power of the corresponding input signal. The two voltages are amplified by a differential amplifier to drive a reflection-mode multiple-quantum-well modulator which is illuminated to produce an output.

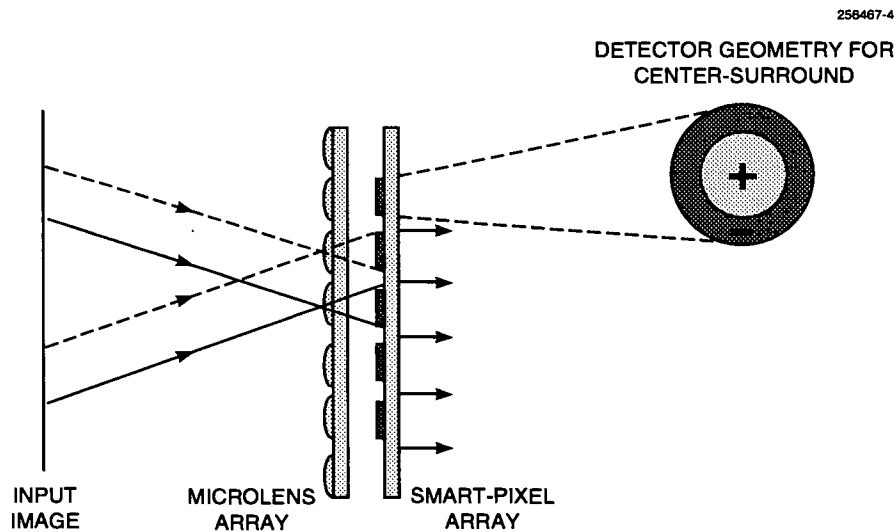


Figure 1-4. First stage of artificial retina implemented using smart-pixel arrays and microlenses.

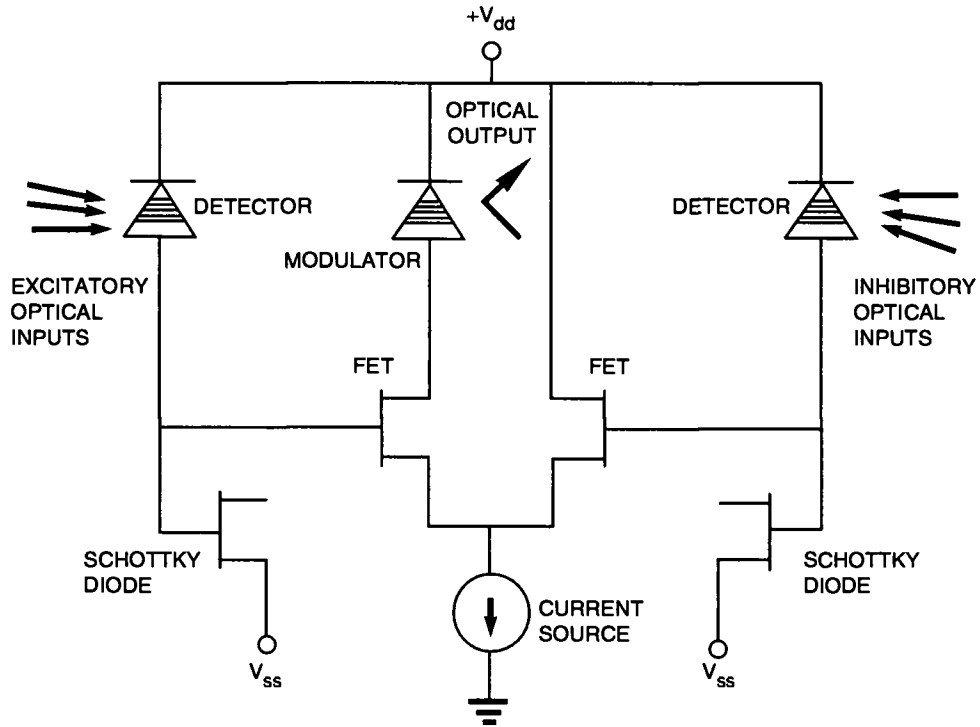


Figure 1-5. Monolithic optoelectronic transistor (MOET) with dual optical inputs. The optical output is a function of the ratio of the power levels of the optical inputs.

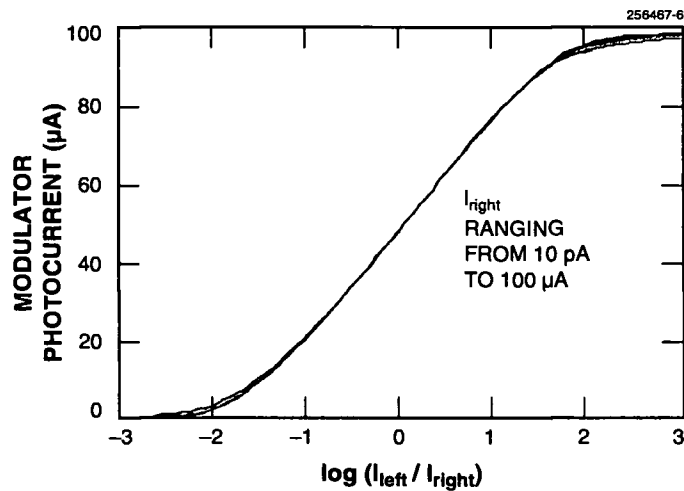


Figure 1-6. Transfer characteristic of MOET. The abscissa is the logarithm of the ratio of the powers of the two optical inputs I_{left} and I_{right} , and the ordinate is the modulator photocurrent, which is proportional to $I-R$, where R is the modulator reflectivity.

The epitaxial structure for the new MOET was grown by gas-source molecular beam epitaxy and consists, in order of growth, of a multilayer dielectric mirror, a layer of p -type AlGaAs, the GaAs/AlGaAs multiple quantum well, and an FET structure that incorporates a n^+ -doped GaAs quantum-well channel. Test structures were fabricated so that the individual components of the circuit could be measured. Data from these measurements were used to extract SPICE parameters for the FET, modulator, and Schottky diode. Figure 1-6 shows the results of SPICE simulation of the circuit. The modulator photocurrent (an inverted measure of optical output) is plotted as a function of the ratio of the two input powers for various absolute power levels on the right-hand detector. The circuit responds to input ratios over nearly four orders of magnitude, and the response curve varies negligibly over seven orders of magnitude of absolute power levels. At very low input powers, leakage currents will limit the response. At high powers, series and spreading resistances in the Schottky diodes will cause a deviation from the logarithmic response.

B. F. Aull
R. J. Poillucci
P. A. Maki

REFERENCES

1. S. H. Groves, J. P. Donnelly, J. N. Walpole, J. D. Woodhouse, L. J. Missaggia, R. J. Bailey, and A. Napoleone, *IEEE Photon. Technol. Lett.* **6**, 1286 (1994).
2. Solid State Research Report, Lincoln Laboratory, MIT, 1994:2, p. 8.
3. J. N. Walpole, E. S. Kintzer, S. R. Chinn, C. A. Wang, and L. J. Missaggia, *Conference on Lasers and Electro-Optics, 1994 Technical Digest Series*, Vol. 8 (Optical Society of America, Washington, D.C., 1994), p. 1.
4. P. S. Yeh, I. F. Wu, S. Jiang, and M. Dagenais, *Electron. Lett.* **29**, 1981 (1993).
5. Solid State Research Report, Lincoln Laboratory, MIT, 1994:2, p. 4.
6. S. R. Chinn, private communication.
7. Solid State Research Report, Lincoln Laboratory, MIT, 1993:2, p. 1.
8. B. F. Aull, K. B. Nichols, P. A. Maki, S. C. Palmateer, E. R. Brown, and T. A. Lind, *Appl. Phys. Lett.* **63**, 1555 (1993).
9. B. F. Aull, Z. L. Liau, P. A. Maki, and E. R. Brown, presented at the IEEE Lasers and Electro-Optics Society Annual Meeting, Boston, Mass., 31 October-3 November 1994.
10. M. Mahowald, *An Analog VLSI System for Stereoscopic Vision* (Kluwer, Norwell, Mass., 1994), p. 4.
11. S. Grossberg and D. Todorovic, in *Neural Networks and Natural Intelligence*, S. Grossberg, ed. (MIT Press, Cambridge, Mass., 1988), p. 127.

2. QUANTUM ELECTRONICS

2.1 ULTRAVIOLET GENERATION WITH PASSIVELY Q -SWITCHED PICOSECOND MICROCHIP LASERS

The generation of coherent ultraviolet (UV) radiation has typically required large, expensive laser systems. By quadrupling the output of a passively Q -switched microchip laser [1], we have demonstrated 0.5- μJ UV pulses of 250-ps duration from a 3-cm-long \times 1-cm-diam package. The device, illustrated in Figure 2-1, is pumped by a 1.2-W fiber-coupled diode laser and operates in a single-frequency, linearly polarized, fundamental transverse mode at pulse repetition rates up to 13 kHz over a temperature range $> 70^\circ\text{C}$.

The passively Q -switched laser used in this device consists of a 1-mm-long piece of 1.8-wt% Nd^{3+} :YAG diffusion bonded to a 0.25-mm-long piece of Cr^{4+} :YAG with an unsaturated absorption coefficient of 0.57 cm^{-1} at $1.064\ \mu\text{m}$. The pump-side face of the Nd:YAG is dielectrically coated to transmit the 808-nm pump light and to be highly reflective at $1.064\ \mu\text{m}$. The output face of the Cr:YAG is 85% reflecting at the oscillating frequency. The 440-ps, 7- μJ /pulse output of the laser is single frequency, linearly polarized, and diffraction limited, with a waist radius of $50\ \mu\text{m}$ and a peak power of 14 kW.

The $1.064\text{-}\mu\text{m}$ output of the microchip laser is frequency doubled with 42% efficiency in a 5-mm-long piece of KTP placed adjacent to the output face of the laser. The output of the KTP is again single frequency, linearly polarized, and diffraction limited. A 5-mm-long BBO crystal placed adjacent to the KTP doubles this radiation with 13% efficiency, resulting in 250-ps, 0.5- μJ , single-frequency, linearly polarized 266-nm UV pulses with a peak power of 1.8 kW.

256467-7

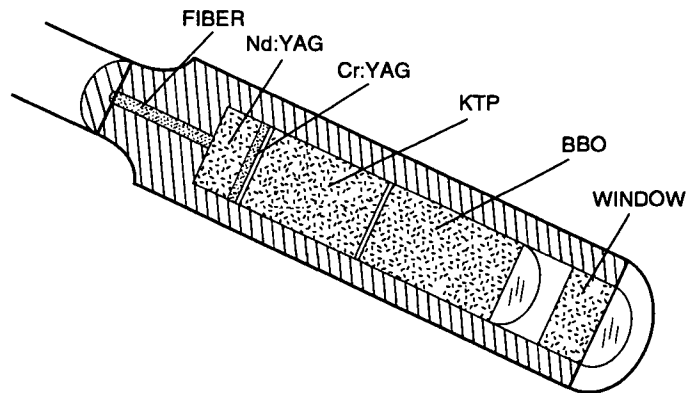


Figure 2-1. Frequency-quadrupled passively Q -switched picosecond microchip laser.

Whereas the 1.064- μm and 532-nm outputs of the laser are circularly symmetric TEM_{00} modes, the 266-nm output has an aspect ratio of 4 to 1 in the far field. This is a result of the small angular acceptance of the BBO in one direction. Consequently, the far-field transverse profile of the 266-nm light is Gaussian in the wide dimension and has an apertured $\sin^2 x/x^2$ dependence in the orthogonal direction.

The short length of the nonlinear crystals used in this device permits efficient frequency conversion over a large temperature window. In addition, the effective temperature window for UV conversion is broadened by the fact that the divergence of the 532-nm light is greater than the acceptance angle of the BBO—at different temperatures different angular portions of the green light are efficiently doubled. As a result, the device has been operated with at least 1 mW of UV output power over a temperature range from 0 to 70°C. The output powers at 1.064 μm , 532 nm, and 266 nm are shown as a function of temperature in Figure 2-2.

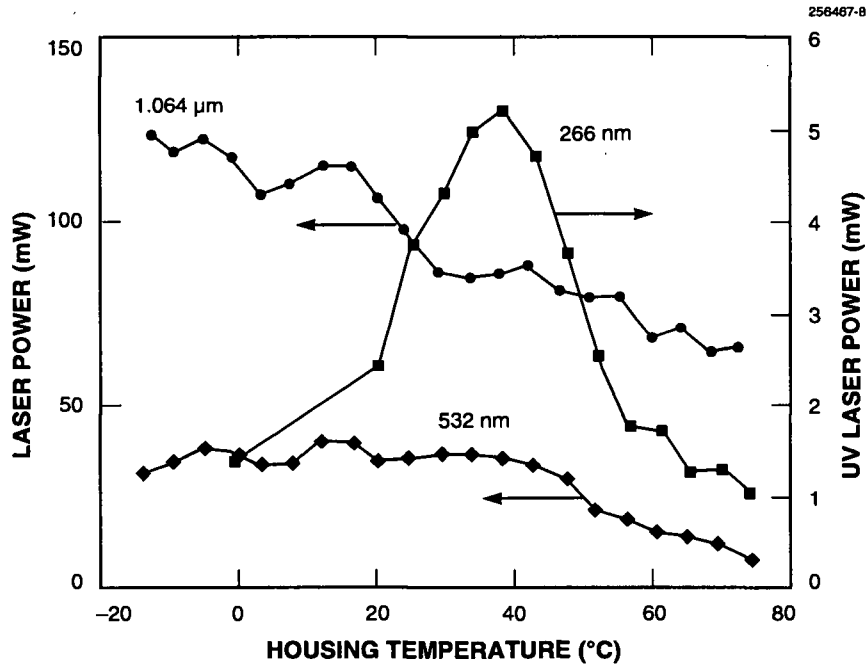


Figure 2-2. Time-averaged output of packaged frequency-quadrupled passively Q -switched picosecond microchip laser at fundamental wavelength (1.064 μm), second harmonic (532 nm), and fourth harmonic (266 nm) as a function of temperature.

Contained within a 3-cm-long \times 1-cm-diam stainless steel package with no electrically active components, the UV microchip laser is extremely robust and can be used in hostile ambient environments. The pulse repetition rate can be controlled by turning the pump diode on and off for each individual output pulse, and the output pulse characteristics are nearly independent of the pulse repetition rate from single shot up to 13 kHz. With all of these features and the potential for low-cost mass production, this UV source should be attractive for applications including UV spectroscopy, environmental monitoring, process control, micromachining, and cellular biology.

J. J. Zayhowski

C. Cook

J. Ochoa

J. L. Daneu

C. Dill III

REFERENCE

1. J. J. Zayhowski and C. Dill III, *Opt. Lett.* **18**, 1427 (1994).

3. MATERIALS RESEARCH

3.1 GROWTH OF GaSb FROM TRIETHYLGALLIUM AND TRISDIMETHYLAMINOANTIMONY

Previously, GaSb has been grown by organometallic vapor phase epitaxy (OMVPE) from triethylgallium (TEGa) and trimethylantimony (TMSb) [1]. Although electrical, optical, and structural properties have indicated high-quality material, these characteristics are temperature dependent because growth is kinetically limited by the thermal decomposition of TMSb. The minimum V/III ratio for obtaining stoichiometric GaSb layers increases with decreasing growth temperature below 600°C. In addition, the use of TMSb for the growth of Al-containing Sb-based alloys is undesirable because of carbon incorporation due to the production of CH₃ radicals. Here, we report on growth of GaSb from TEGa and a new Sb source, trisdimethylaminoantimony (TDMASb) [Sb(N(CH₃)₂)₃], which is a thermally less stable group V source and should not promote carbon incorporation [2],[3].

The GaSb epilayers were grown in a vertical rotating-disk OMVPE reactor operated at 0.2 atm. The source materials were electronic grade TEGa and research grade TDMASb. The carrier gas was H₂ at a flow rate of 10 slpm. The TEGa mole fraction was 1×10^{-4} while the TDMASb mole fraction ranged from 0.6 to 1×10^{-4} . The flow of TDMASb was calculated with the assumption that the vapor pressure of TDMASb is ~ 0.7 Torr at 25°C. This value was based on Epison [4] measurements of the sound velocity of the TDMASb/H₂ mixture compared to that of pure H₂. It should be noted that the reported vapor pressure of TDMASb varies from 0.45 Torr at 32 to 34°C [5] to 2.6 Torr at 25°C [6].

The TEGa and TDMASb sources were premixed in a fast switching manifold before introduction into the reactor. The GaSb growth temperature was varied from 450 to 575°C. GaSb epilayers were grown on Te-doped GaSb substrates, (100) oriented 2° toward (110), or on semi-insulating GaAs substrates for electrical measurements. During growth the sample was illuminated with the beam from a He-Ne laser, and the diffuse scattering from the sample surface was monitored. In a separate series of experiments, Fourier transform infrared (FTIR) spectra of TEGa and TDMASb were measured in a specially designed gas cell to study gas phase reactions [3].

Figure 3-1 shows the surface morphology of a typical GaSb epilayer grown with TEGa and TDMASb. The layer exhibited a mirror surface to the eye. At the top of the micrograph, which corresponds to the edge of the wafer, the surface was featureless. However, the lower portion shows some surface contamination. Chemical analysis by Auger spectroscopy indicates the product contains both Ga and Sb, and possibly N. (The presence of small amounts of N cannot be detected in the presence of antimony.) Since the intensity of diffuse scattering from the wafer surface was weak during growth, but then increased abruptly upon termination of growth and cooling of the wafer, we believe the degraded surface morphology results from post-growth deposition of volatile adducts that form between TEGa and TDMASb. Additional evidence for adduct formation is the observation of a clear liquid that condensed at the inlet to our reactor from the gas mixing manifold.

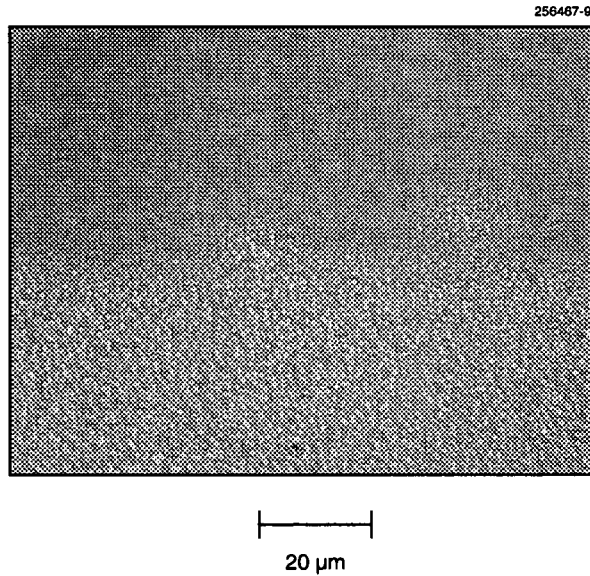


Figure 3-1. Surface morphology of GaSb layer grown with TEGa and TDMASb; $T = 575^{\circ}\text{C}$ and $V/III = 1$.

Further insight into the pre-reactions that result from the direct mixing of TEGa and TDMASb is obtained from FTIR under static conditions. Figure 3-2 shows the steady-state IR spectra measured at room temperature and atmospheric pressure for TEGa, TDMASb, and a mixture of TEGa and TDMASb. Infrared analysis of this mixture indicates that the gas phase consists of $\text{Ga}(\text{N}(\text{CH}_3)_2)(\text{C}_2\text{H}_5)_2$ and $\text{Sb}(\text{N}(\text{CH}_3)_2)_x(\text{C}_2\text{H}_5)_{3-x}$ ($x = 1, 2$). The appearance of these products indicates ligand exchange reactions between TDMASb and TEGa via formation of Lewis acid-base adducts. Such pre-reactions may be minimized by keeping the TEGa and TDMASb flows separated until introduction into the reactor.

The minimum V/III ratio required for the growth of stoichiometric GaSb is shown in Figure 3-3 as a function of growth temperature. For values below the line, gallium droplets were observed. For the temperature range between 500 and 575°C , the V/III ratio is constant at 0.7, which indicates that the thermal decomposition of TDMASb is complete. For a growth temperature $< 500^{\circ}\text{C}$, the V/III ratio decreased as a result of the incomplete decomposition of TEGa.

GaSb layers were *p*-type with a typical room-temperature hole concentration of $4.6 \times 10^{17} \text{ cm}^{-3}$ and hole mobility of $370 \text{ cm}^2/\text{V s}$. These values are greatly inferior to our previously reported values for GaSb [1], but are not surprising since the TDMASb is an experimental source and is not electronic grade. Figure 3-4 shows the double-crystal x-ray diffraction spectra for GaSb layers grown from TEGa and TDMASb, and TEGa and TMSb. For the layer grown with TDMASb as the Sb source, the epilayer peak is shifted to larger diffraction angles with respect to the substrate peak (~ 165 arc sec), which indicates that the epilayer has a smaller lattice constant. A possible explanation is that N is incorporated in the epilayer as a result of ligand exchange reactions between TEGa and TDMASb. The concentration of N

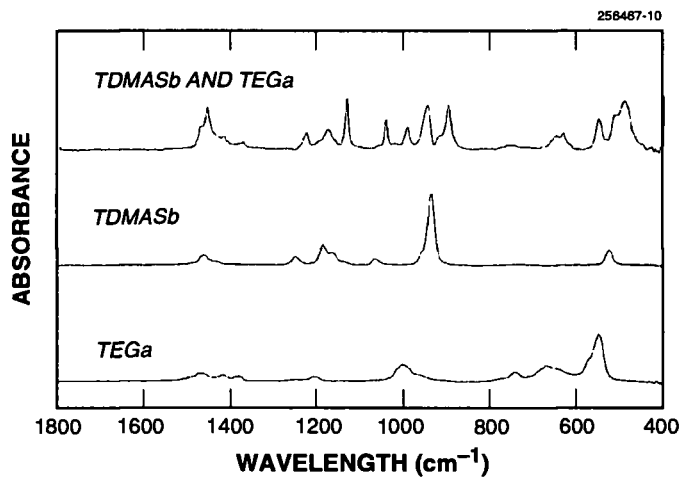


Figure 3-2. Fourier transform infrared absorption spectra of TDMASb and TEGa, TDMASb, and TEGa.

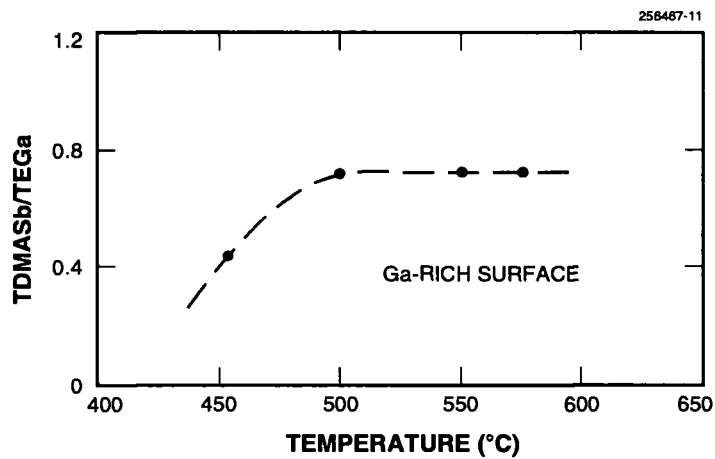


Figure 3-3. Minimum VIII ratio for stoichiometric growth of GaSb grown with TDMASb and TEGa.

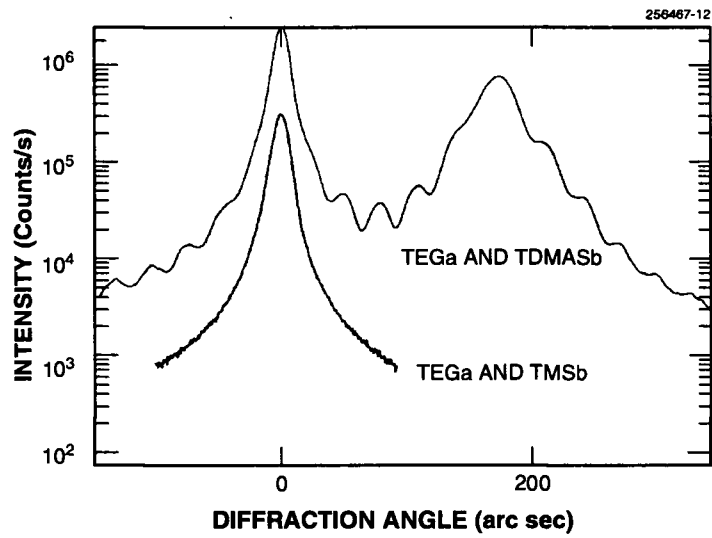


Figure 3-4. Double crystal x-ray diffraction curve of GaSb grown on GaSb substrate by TEGa and TDMASb, and TEGa and TMSb.

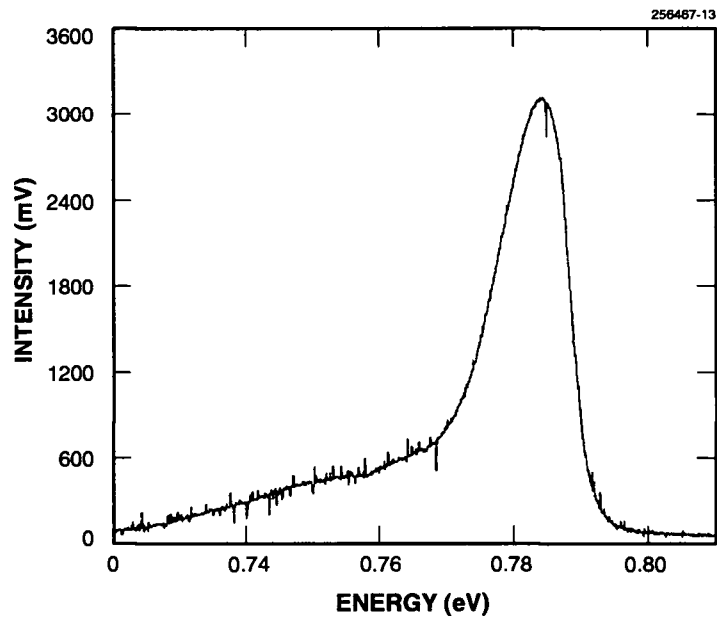


Figure 3-5. Low-temperature photoluminescence spectrum of GaSb.

is estimated to be approximately 0.4% based on the cubic lattice constant of GaN (0.454 nm) and Vegard's law. Secondary ion mass spectroscopy is needed to confirm the incorporation of N. Similar observations have been reported for AlGaAs grown with trisdimethylaminoarsine [7]. The low-temperature photoluminescence spectrum shown Figure 3-5 consists of a broad peak centered around 0.78 eV.

C. A. Wang	S. Salim*
J. H. Reinold	K. F. Jensen*
M. C. Finn	A. C. Jones*
D. R. Calawa	

3.2 TRITERTIARYBUTYLALUMINUM AS A NEW ORGANOMETALLIC SOURCE FOR EPITAXIAL GROWTH OF AlGaSb

A new organometallic source, tritertiarybutylaluminum (TTBAI), has been used for the first time in the growth of AlGaSb by low-pressure OMVPE. AlGaSb and its related alloys grown on GaSb or InAs substrates are useful materials for diode lasers and detectors which operate in the wavelength range between 2 and 5 μm . However, OMVPE growth of AlGaSb for such devices has been problematic because conventional methyl-based precursors result in high incorporation levels of carbon that lead to high hole concentrations that cannot be compensated by *n*-type dopants. TTBAI has been reported to yield Al films with low carbon levels [8] and therefore is of interest as an Al source for the growth of Al-based III-V compound semiconductors.

Epitaxial layers were grown simultaneously on (100) GaSb and semi-insulating (100) GaAs substrates, misoriented 2° toward (110), in a vertical rotating-disk reactor operated at 150 Torr. TTBAI, TEGa, and TMSb were used as organometallic sources. The organometallics were held in temperature baths maintained at 24°C for TEGa and TTBAI and 0° for TMSb. Vapor pressure data for TEGa and TMSb were obtained from the literature [9]. However, since little information is available on the vapor pressure of TTBAI, a value of 0.5 Torr at 24°C was estimated from Epison [4] measurements of the sound velocity of the TTBAI/H₂ mixture compared to that of pure H₂. The growth temperature was 550°C and V/III ratios varied between 2.8 and 3.6. AlGaSb epilayers were capped with a thin (~ 20 nm) GaSb layer to facilitate ohmic contact formation. Typical epilayer thickness was 1.5 μm .

The surface morphology was examined by Nomarski contrast microscopy. The alloy composition of Al_xGa_{1-x}Sb layers (*x* > 0.2) was determined by Auger electron spectroscopy sputter profiles based on GaSb and AlSb standards, or from the near band-edge photoluminescence measured at 4 K and the energy-composition dependent relationship [10] $E_g(x) = 0.813 + 1.097x + 0.40x^2$. Carrier concentration and mobility at 77 K were determined from Hall measurements based on the van der Pauw method on etched cloverleaf structures. In addition, in-situ FTIR measurements were performed in a separate series of experiments to study gas phase reactions in the reactor [3].

*Author not at Lincoln Laboratory.

Figure 3-6 shows Nomarski micrographs of $\text{Al}_x\text{Ga}_{1-x}\text{Sb}$ ($0 < x \leq 1$) epilayers grown on GaSb substrates. For all layers the surface morphology was mirror and showed no degradation with increasing x , contrary to observations for growth of AlGaSb with trimethylaluminum as the Al source [11]. For $x < 0.2$, the morphology was featureless, and for $x > 0.2$ the layers exhibited crosshatching because of the lattice mismatch between the epilayer and the GaSb substrate.

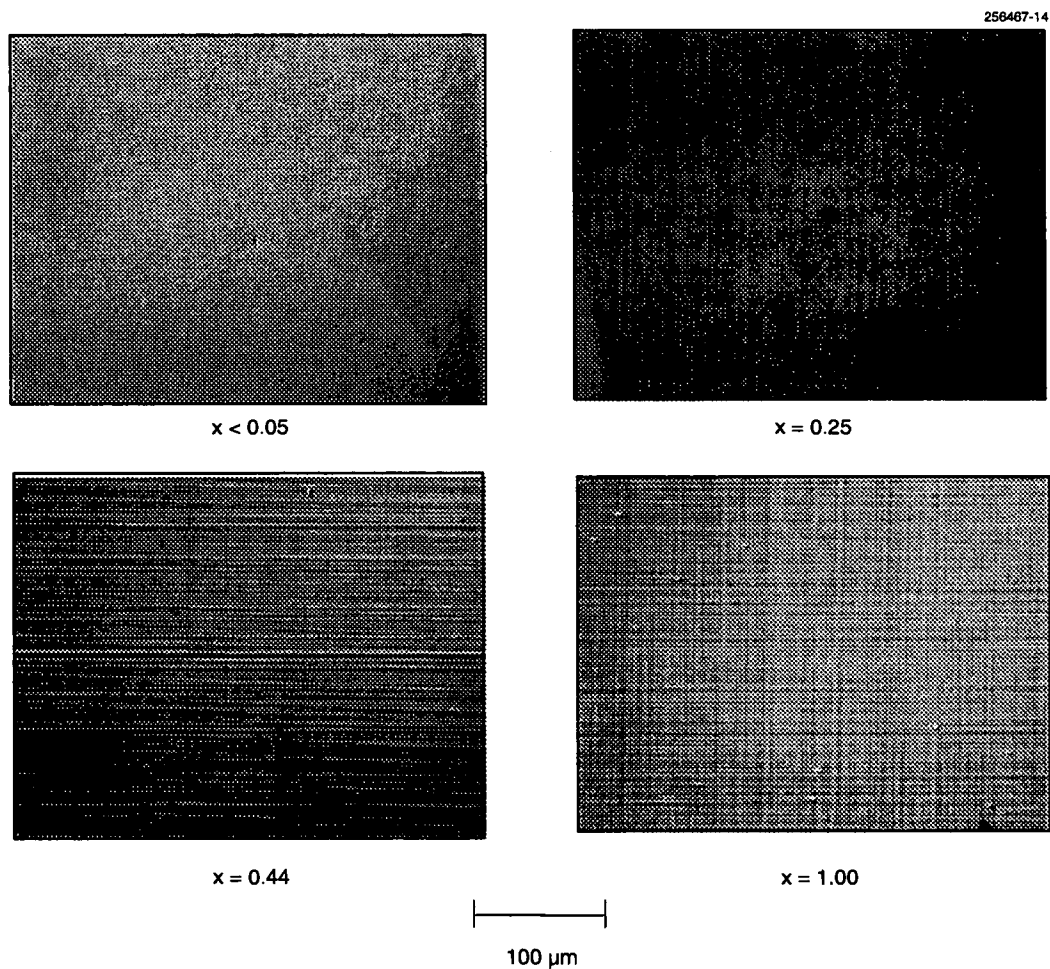


Figure 3-6. Surface morphology of $\text{Al}_x\text{Ga}_{1-x}\text{Sb}$ layer grown at $T = 550^\circ\text{C}$.

The dependence of AlSb incorporation in AlGaSb on TTBAI in the vapor phase is shown in Figure 3-7, where x_{vapor} is defined as the ratio of the TTBAI mole fraction to the total group III mole fraction. The Al distribution coefficient $k_{\text{Al}} = x_{\text{solid}}/x_{\text{vapor}}$ is less than unity. A possible explanation is that TTBAI forms an adduct with TMSb and is not incorporated into the film. In another set of experiments, in-situ FTIR spectra indicated chemical reactions between TTBAI and TMSb. Such pre-reactions could explain our observation that k_{Al} decreased as the V/III ratio increased. It is also noted that GaSb growth at 550°C requires a minimum V/III ratio of 1.8, whereas for AlGaSb growth a value greater than 2.2 is required, which increases with x_{vapor} .

Over the whole composition range all of these unintentionally doped $\text{Al}_x\text{Ga}_{1-x}\text{Sb}$ layers were *p*-type. As shown in Figure 3-8(a), the hole concentration at 77 K increased rapidly from $8 \times 10^{15} \text{ cm}^{-3}$ for $x = 0.02$ to $8 \times 10^{17} \text{ cm}^{-3}$ for $x = 0.44$, and then gradually increased with x and was a maximum value of $3.8 \times 10^{18} \text{ cm}^{-3}$ for $x = 1$. The corresponding hole mobility shown in Figure 3-8(b) decreased considerably with x . This decrease is a consequence of both higher AlSb alloy composition and higher hole concentration. The hole mobility vs concentration is shown in Figure 3-9 for our data and for the only other data published for AlGaSb grown by OMVPE [12].

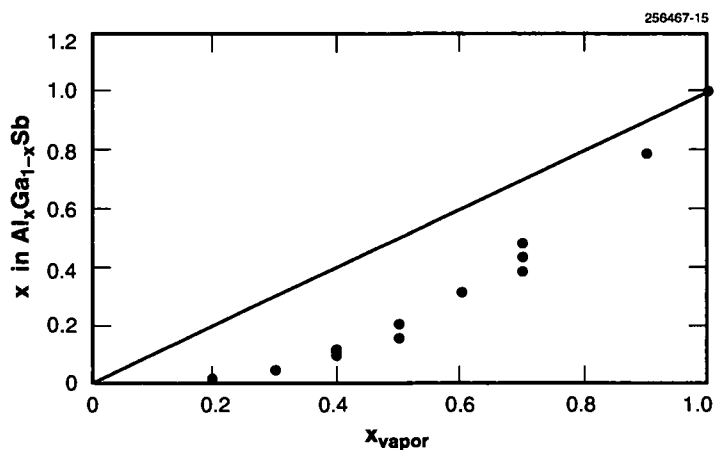


Figure 3-7. Dependence of AlSb incorporation on TTBAI vapor phase composition where x_{vapor} is the ratio of the TTBAI mole fraction to the total group III (TTBAI and TEGa) mole fraction.

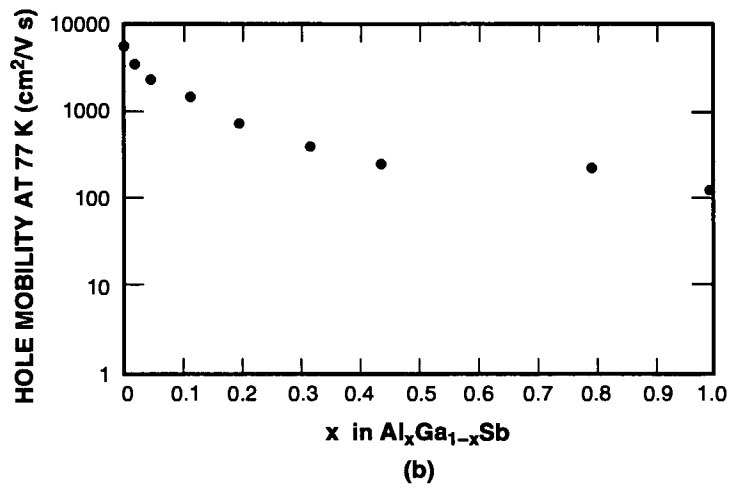
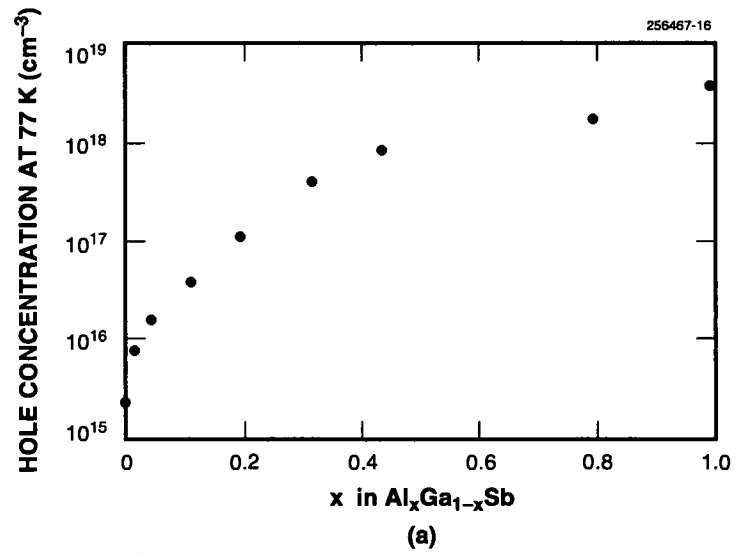


Figure 3-8. Variation of (a) hole concentration and (b) hole mobility at 77 K with AlSb composition.

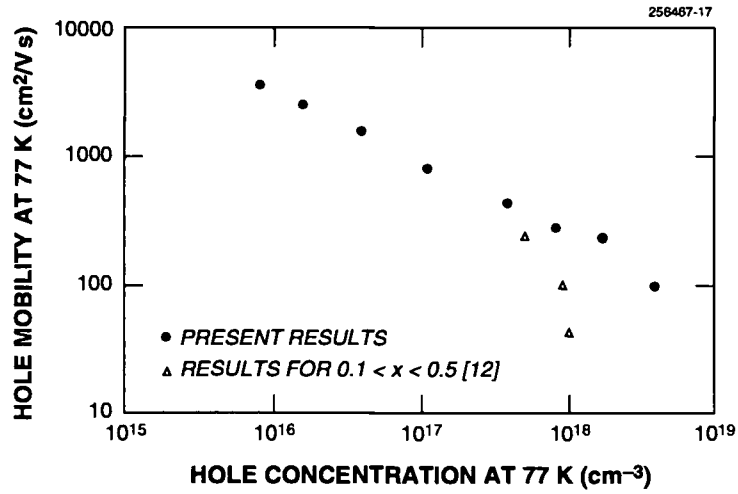


Figure 3-9. Hole mobility vs concentration for $Al_xGa_{1-x}Sb$ grown by organometallic vapor phase epitaxy.

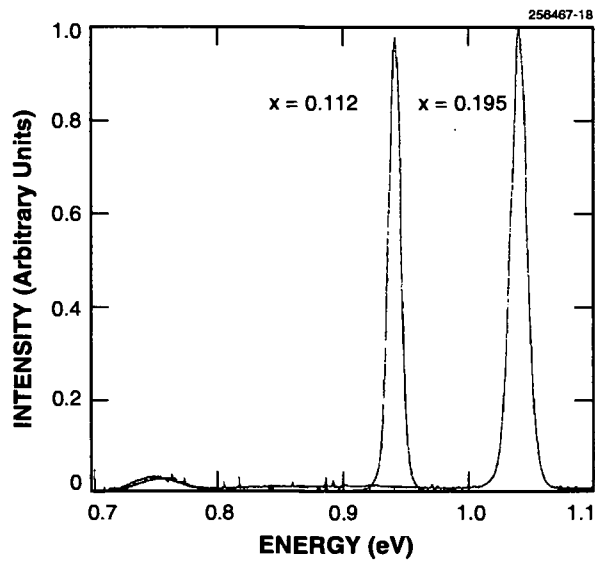


Figure 3-10. Low-temperature photoluminescence spectra of $Al_xGa_{1-x}Sb$.

Photoluminescence at 4 K was observed for $\text{Al}_x\text{Ga}_{1-x}\text{Sb}$ layers with $x < 0.2$. The crossover between the Γ and X bands is reported to occur at $x = 0.21$ [10]. Representative spectra for two samples grown on GaSb substrates are shown in Figure 3-10 for $x = 0.1$ and 0.2. The spectra have the common feature of a single peak with a full width at half-maximum of 11.4 and 15 meV, respectively.

C. A. Wang	S. Salim*
J. H. Reinold	K. F. Jensen*
M. C. Finn	A. C. Jones*
J. W. Chludzinski	

REFERENCES

1. Solid State Research Report, Lincoln Laboratory, MIT, 1994:2, p. 30.
2. J. Shin, A. Verma, G. B. Stringfellow, and R. W. Gedridge, Jr., *J. Cryst. Growth* **143**, 15 (1994).
3. S. Salim, Ph.D. thesis, Massachusetts Institute of Technology, 1995.
4. Thomas Swan and Co. Ltd., Cambridge, United Kingdom.
5. K. Mordritzer, *Inorg. Chem.* **3**, 609 (1964).
6. K. C. Baucom and R. M. Biefield, *Appl. Phys. Lett.* **64**, 3021 (1994).
7. G. Zimmermann, H. Protzmann, T. Marschner, O. Zsebok, W. Stolz, E. O. Gobel, P. Gimmnich, J. Lorberth, T. Filz, P. Kurpas, and W. Richter, *J. Cryst. Growth* **129**, 37 (1993).
8. A. C. Jones, J. Auld, S. A. Rushworth, and G. W. Critchlow, *J. Cryst. Growth* **135**, 285 (1994).
9. G. B. Stringfellow, *Organometallic Vapor Phase Epitaxy: Theory and Practice* (Academic, New York, 1989).
10. J. Allegre, M. Averous, and A. Joullie, *J. Lumin.* **17**, 301 (1978).
11. D. S. Cao, Z. M. Fang, and G. B. Stringfellow, *J. Cryst. Growth* **113**, 441 (1991).
12. E. T. R. Chidley, S. K. Haywood, R. E. Mallard, N. J. Mason, R. J. Nicholas, P. J. Walker, and R. J. Warburton, *J. Cryst. Growth* **93**, 70 (1988).

*Author not at Lincoln Laboratory.

4. SUBMICROMETER TECHNOLOGY

4.1 NITROGEN-ARRIVAL-RATE-LIMITED GROWTH OF GaN USING AN ELECTRON-CYCLOTRON-RESONANCE DISCHARGE SOURCE IN GAS-SOURCE MOLECULAR BEAM EPITAXY

Recent advances in the growth of GaN by molecular beam epitaxy (MBE) have occurred because of the availability of compact nitrogen plasma sources such as electron-cyclotron-resonance (ECR) discharge sources, which generate significant quantities of atomic nitrogen from diatomic nitrogen gas using an ECR plasma-assisted decomposition process. Previous studies [1]-[4] of ECR-MBE GaN growth have apparently been under nitrogen-rich conditions, resulting in residual *n*-type GaN. In the present work, we demonstrate a gallium-rich growth regime whereby the growth rate is determined by the nitrogen flux from the ECR source, with excess gallium evaporating from the growth surface. Under these conditions, the growth rate is relatively insensitive to the gallium flux and, furthermore, the morphology of the epitaxial film does not show excess gallium droplets usually characteristic of gallium-rich growth conditions. These conditions are found to significantly reduce the *n*-type residual conduction characteristics of the films and produce high-resistivity films that can be silicon doped to obtain *n*-type material.

The growth system in these experiments is a gas-source MBE machine equipped with a compact ECR source with a source aperture. The gallium beam is generated by a conventional thermal effusion source. ULSI-grade nitrogen is purified using a Nanochem purifier. All the growths reported here are on basal plane sapphire at a substrate thermocouple temperature of 950°C. The characterization of the ion species from the ECR source is made using a quadrupole mass analyzer, operated with the ionizer filament current off. The analyzer is mounted in a direct line of sight to the ECR source. In this mode, ions generated by the ECR source are captured in the ionizer assembly, extracted and injected into the quadrupole mass filter, and subsequently detected using a faraday cup and an electron multiplier. This technique provides a simple method for detecting ECR source instabilities and optimizing the ECR source conditions. In particular, the magnet current must be set such that the ECR condition is attained. Here, we use the residual gas analyzer to determine this condition by varying the magnet current such that the ion intensities from the source are maximized, as described below. We assume that this corresponds to a magnetic field that satisfies the ECR condition at 2.45 GHz.

Figure 4-1 shows a typical ion spectrum at a nitrogen mass flow of 3.3 sccm and a net RF power of 20 W ($P_{\text{forward}} - P_{\text{reflected}}$). The ECR magnet current is set by maximizing the mass 28 (N_2^+) ion current. In addition to the expected N_2^+ (mass 28) and N^+ (mass 14), two other nitrogen species are observed. These are mass 7, which we attribute to N^{++} , and mass 42, which we attribute to N_3^+ . The two remaining species observed, Ar^+ (mass 40) and Ne^+ (mass 20), are typical contaminants of commercially available nitrogen gas and liquid obtained through the cryogenic distillation process. The residual species are not important to the growth process itself but may have significant bearing on the electronic properties of the material.

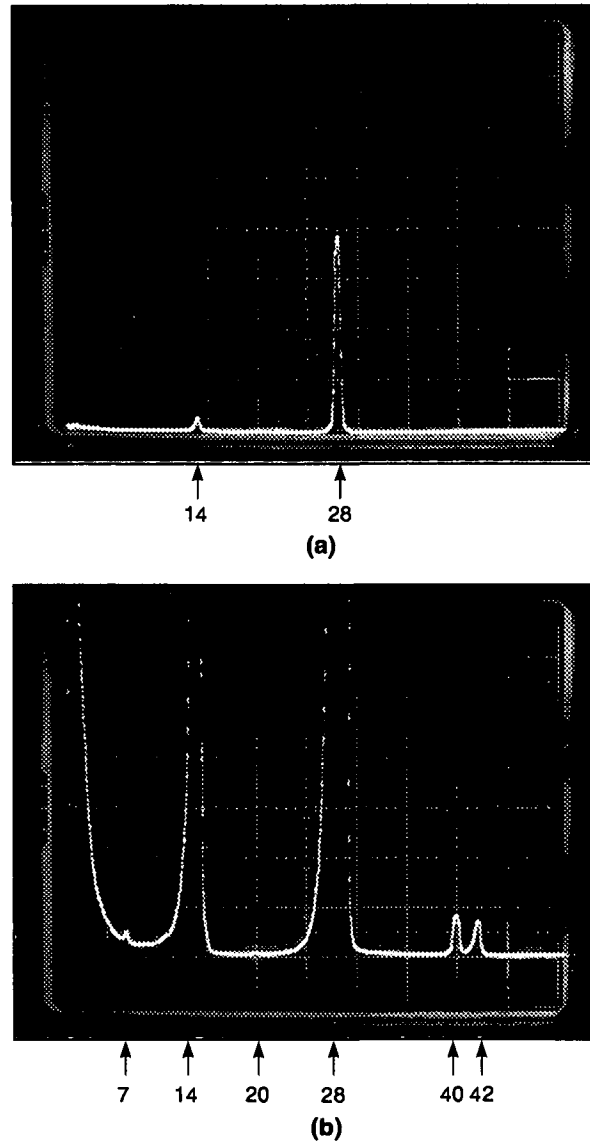


Figure 4-1. Ion spectrum as measured by quadrupole mass analyzer with ionizer filament current off: (a) Spectrum showing ions at 14 amu (N^+ or N_2^{++}) and 28 amu (N_2^+) peaks; (b) same spectrum as in (a) but magnified 250 times, showing 7 amu (N^{++}), 20 amu (Ne^+), 40 amu (Ar^+), and 42 amu (N_3^+), as well as 14 and 28 amu peaks. The horizontal scan covers a mass-to-charge ratio of 0 to 50 amu. The N_2 mass flow is 3.3 sccm, and the RF net power is 20 W.

Figure 4-2 shows the dependence of the ion spectrum on nitrogen mass flow at a net RF power of 20 W. The general trend for all the species, except N_3^+ , is a gradual increase in the ion current as the N_2 mass flow is decreased from 6.6 to 3.3 sccm, with the current maximized at 3.3 sccm. After the peak at 3.3 sccm, the ion current decreases rapidly as the mass flow is decreased. The exception to this behavior is the N_3^+ ion current, which monotonically decreases from 6.6 to 1.6 sccm.

An explanation for the ion current peak at 3.3 sccm can be deduced by analyzing the GaN growth rate dependence on nitrogen mass flow. Figure 4-3 shows the dependence of the growth rate of GaN at a fixed gallium flux and a net RF power of 20 W, as a function of nitrogen mass flow. (Also plotted for comparison are the normalized N_2^+ and N^+ ion currents.) The growth rate increases from 380 Å/h at 6.6 sccm up to 610 Å/h at 3.3 sccm, remains relatively constant at 580 Å/h at 1.6 sccm, and then drops rapidly to 140 Å/h at 0.7 sccm. These data combined with the ion flux data shown in Figure 4-2 indicate that the following conditions are probably occurring. The higher flow regime of 6.6 sccm corresponds to a higher background pressure ($\sim 1.2 \times 10^{-4}$ Torr) in the growth chamber, with a correspondingly shorter mean free path for the growth gases. The reduced growth rate occurs because either the gallium flux or the nitrogen flux is reduced because of collisions with background molecules on the normally ballistic trajectories from the sources to the substrate.

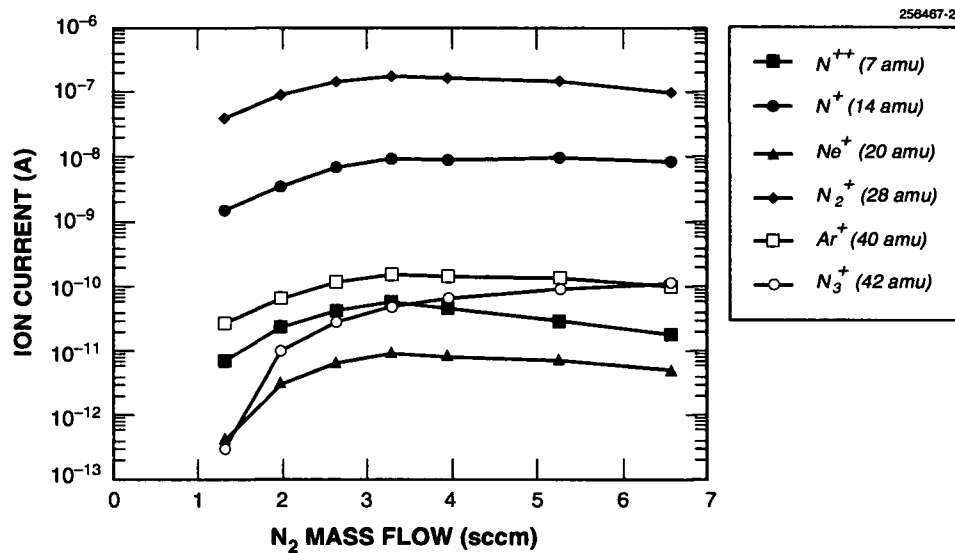


Figure 4-2. Ion current as function of N_2 mass flow for ion species indicated in Figure 4-1. The electron-cyclotron-resonance (ECR) RF net power is 20 W.

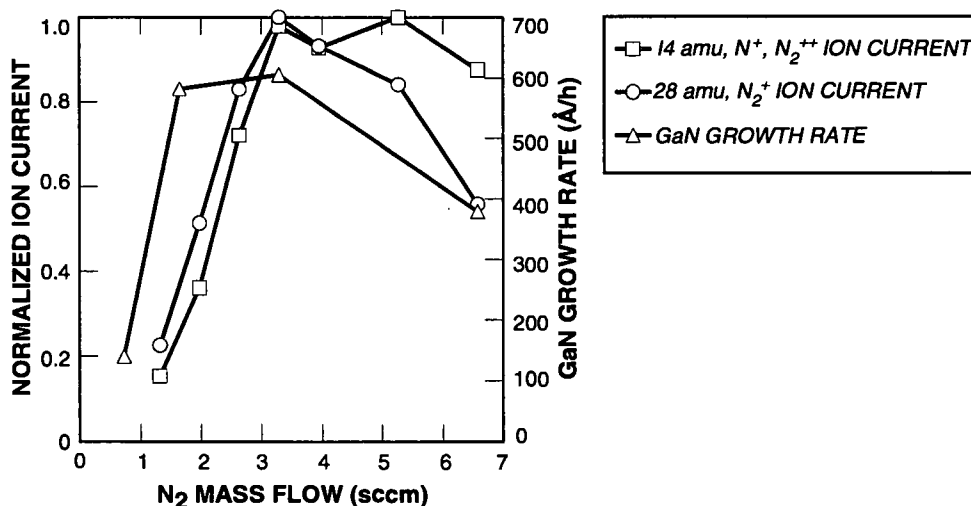


Figure 4-3. Normalized 14- and 28-amu ion currents and GaN growth rate, plotted as function of N₂ mass flow. The ECR RF net power is 20 W.

This explanation is consistent with the ion flux data, since the primary species are all increasing as the mass flow decreases. It is also consistent with the decreasing N₃⁺ flux, as this species can only be formed by a gas phase collision process between the primary species, the probability of which is reduced as the pressure is reduced. Below 3.3 sccm the decrease in growth rate can only be explained by a reduced nitrogen flux, with excess gallium evaporating from the surface. The explanation is consistent with the ion flux data as well. An important species for growth, neutral atomic nitrogen, is not detectable by this method, but judging by the growth rate data this species must follow the general trend of the ion species. The evaporation of excess gallium, which is indicated by the absence of nucleated gallium droplets, is favored by the high substrate temperature (950°C). This is an unusual MBE growth regime, and to the best of our knowledge, is the first demonstration of group-V-limited (nitrogen-limited) growth conditions in the III-V compounds.

The insensitivity of the growth rate to the gallium flux is further illustrated in Figure 4-4, which combines the data obtained at several nitrogen mass flows and gallium fluxes. The flux data have been normalized to the GaN monolayer atomic density, based on flux calibrations determined using reflection electron diffraction (RED) oscillations on GaAs to measure the absolute flux density. From this calibration it is apparent that all the growths reported here are under conditions of excess gallium flux. Furthermore, the growth rate is independent of the gallium flux to within experimental error, as indicated by the wide range of data at mass flows of 3.3 and 6.6 sccm. Also included in the figure is the result of a recent growth at an increased RF power of 38 W and a mass flow of 3.3 sccm, which resulted in an increase in growth rate by a factor of 2.4. This indicates that the RF power is determining the nitrogen generation rate and thereby the GaN growth rate, at least at 3.3-sccm flow conditions.

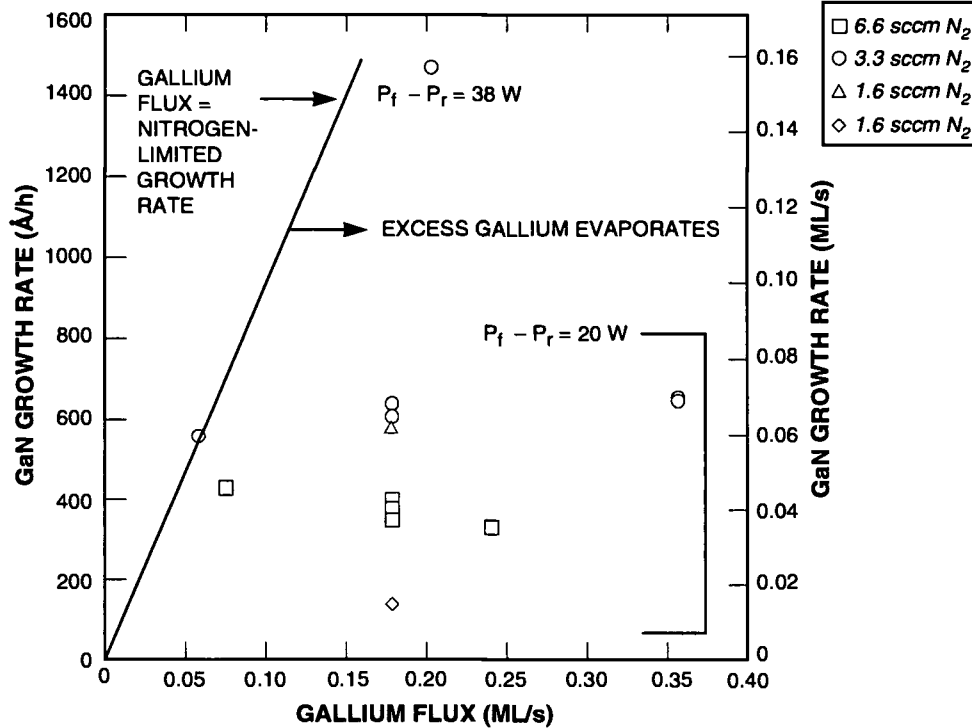


Figure 4-4. GaN growth rate as function of gallium flux and N_2 mass flow, normalized to GaN (0001) plane monolayer (ML) gallium density. For convenience, the growth rate is expressed in both $\text{\AA}/h$ and ML/s. Indicated on the figure is the line where the Ga flux equals the GaN growth rate. All data below $800 \text{\AA}/h$ are at a net RF power of 20 W.

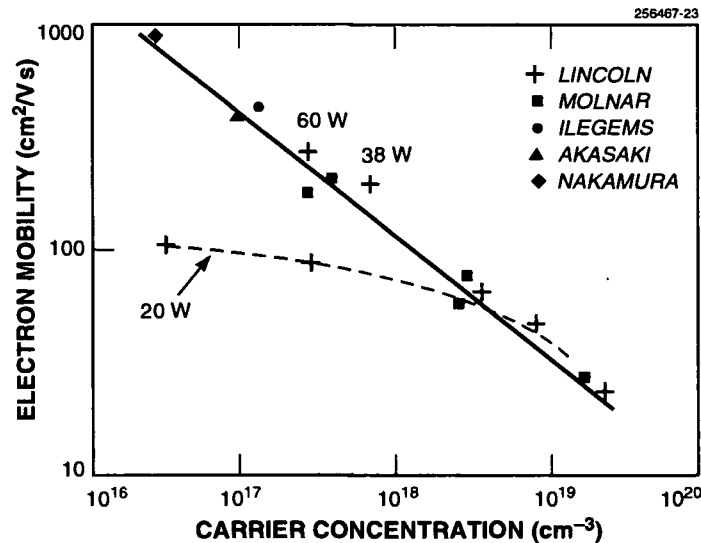


Figure 4-5. Survey of undoped GaN electron mobilities as function of carrier concentrations from Molnar et al. [5] and references therein. Also included are the present Lincoln results at RF powers of 20 W (dashed line) and 38 and 60 W (single data points). The solid line is drawn to aid the eye.

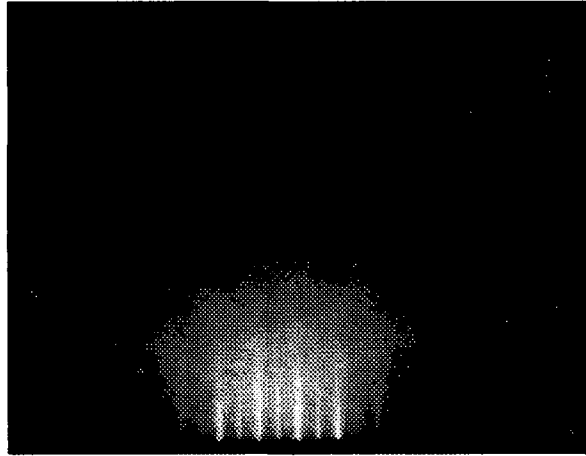


Figure 4-6. 20-keV Reflection electron diffraction pattern from GaN along the $[2\bar{1}10]$ direction grown on (0001) sapphire. The substrate temperature is 950°C , and the nitrogen plasma beam is on.

Finally, the significance of this growth regime is evident from the GaN electronic properties. Previous studies have reported that GaN is either residually n -type, because of nitrogen vacancies, or insulating and unaffected by intentional doping. We have obtained materials that are residually n -type and compare favorably with published results [1],[5],[6] ($n_{300} \approx 2.5 \times 10^{17} \text{ cm}^{-3}$ and $\mu_{300} \approx 270 \text{ cm}^2/\text{V s}$), as shown in Figure 4-5, and by increasing the gallium flux we have also successfully doped insulating materials with silicon to obtain n -type material ($n_{300} \approx 1.2 \times 10^{17} \text{ cm}^{-3}$ and $\mu_{300} \approx 65 \text{ cm}^2/\text{V s}$). These are some of the highest mobilities reported for silicon-doped GaN grown by ECR MBE. The results suggest that the nitrogen-limited growth conditions reported here will be important for successful p doping of GaN, which has proven to be more difficult. Furthermore, these conditions produce high-crystalline-quality material, as shown in the RED pattern in Figure 4-6.

P. A. Maki

4.2 COLOR SEPARATION ECHELON GRATINGS

Color discrimination by wavelength bands has a large number of military and commercial applications. In the infrared portion of the spectrum, wavelength separation allows better temperature discrimination of thermally emissive objects. In the visible portion of the spectrum, a device that separates white light into red, green, and blue wavebands without loss of energy could increase the efficiency of color sensors and color projection displays. As shown in Figure 4-7, an echelon-like grating structure [7] separates electromagnetic (EM) radiation of different wavelengths according to diffraction order rather than by dispersion within one diffraction order as would be the case for a conventional prism-type grating.

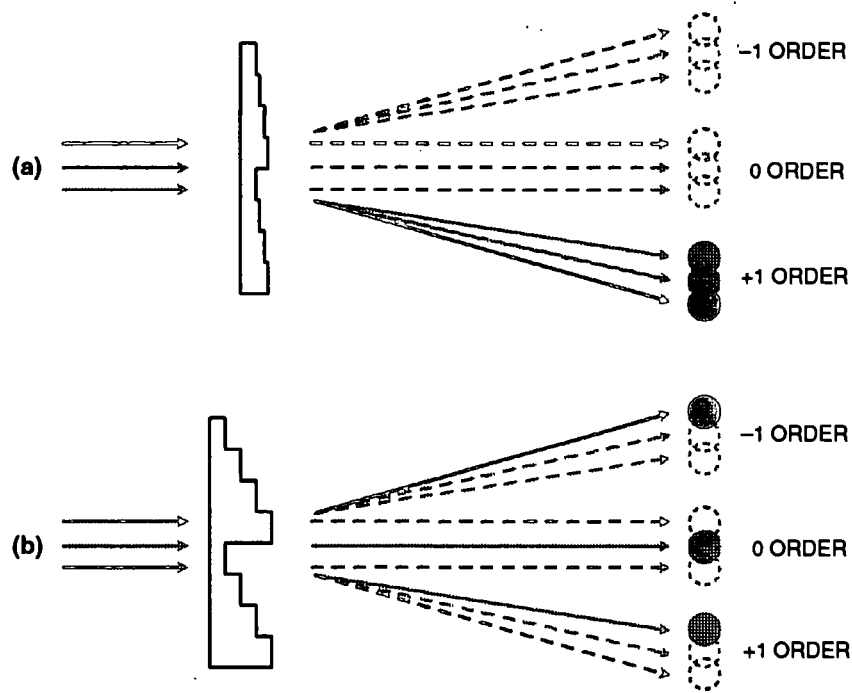


Figure 4-7. Color separation by dispersion in (a) conventional stepped grating and (b) binary optics echelon grating.

A binary optics “echelon” grating structure designed for a color liquid-crystal direct-view projection display has been fabricated in fused silica. This grating disperses red light (700 nm) into the -1 order, green light (525 nm) into the 0 order, and blue light (420 nm) into the $+1$ order. When combined with a collimated illuminator and a microlens array, it produces arrays of red, blue, and green spots that can be individually controlled by liquid-crystal light valves to form a displayed image.

The echelon grating consists of N steps, each of which has a physical depth $d = \lambda_0 / (n_0 - 1)$, where the grating depth d is determined by the wavelength λ_0 at which the zero-order diffraction efficiency is maximized. The period T is determined by the design wavelength, the number of steps, and the desired lateral separation between wavebands. The display application requires a 75×60 -mm grating area (96-mm diagonal), a $4\text{-}\mu\text{m}$ grating period, and a four-phase-level profile. The gratings are fabricated in 100-mm fused silica wafers (25-mil thickness) using the binary optics process, which is shown in Figure 4-8. For a design wavelength of 525 nm and an index of refraction n_0 of 1.46, each of the $1\text{-}\mu\text{m}$ -wide steps is $1.14\text{ }\mu\text{m}$ deep, for a total etch depth of $3.42\text{ }\mu\text{m}$.

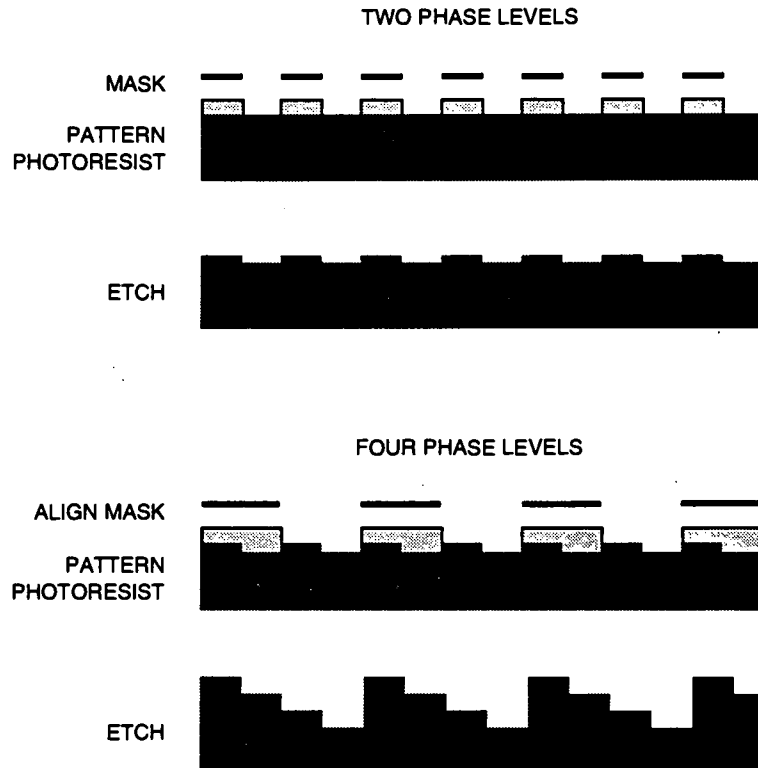


Figure 4-8. Schematic diagram showing two lithographic steps required to fabricate a binary optics component with four phase levels. This sequence can be generalized to fabricate 2^M phase levels using M lithographic steps.

The gratings were fabricated in our Microelectronics Laboratory using the 4-in. Si processing equipment. As might be expected, great ingenuity was required to process transparent, nonconducting wafers without modifying the Si-based equipment. Al-coated fused silica wafers were exposed on the 5 \times reduction i-line optical stepper. Four rows of five 15-mm-square grating blocks were stepped across the wafer to create the 75 mm (x) \times 60 mm (y) continuous patterned area. Stitching errors in the y -direction ranged between 0.2 and 1 μm . Strict control of both exposure and development parameters are needed to achieve the 50% duty cycle required for these binary optics gratings. A 1- μm -thick positive photoresist was used for the first mask layer (2- μm -period grating) and a 2- μm -thick photoresist was used for the second mask layer (4- μm -period grating). Thicker resist was needed to planarize the previously etched 1.14- μm -deep structures. Overlays better than 0.2 μm ($0.15 \pm 0.1 \mu\text{m}$ for a test pattern) were achieved on the stepper using global alignment across the 4-in. wafer. (The full coverage of the pattern precluded local alignment.)

Following a wet-chemical Al etch, the substrates are mounted on 4-in. Si carrier wafers and then etched in a parallel-plate reactive ion etching (RIE) system to the target depth. To achieve the desired anisotropic profile, samples are etched at 20°C in a $\text{CF}_4/\text{CHF}_3/\text{He}$ mixture at a pressure of 300 mTorr and RF power of 350 W at an etching rate of about 62 Å/s. Selectivity between the photoresist mask and the quartz substrate is approximately 2.5:1. Etch depths are controlled by etch time. The RIE system can achieve better than 3% uniformity over the central 75-mm-diam region of Si wafers coated with thermal silicon dioxide. In an initial attempt to monitor the RIE process, the etch depth of 25- μm -wide witness etch features was measured at locations adjacent to the grating area with a stylus profilometer. However, an enormous variation (> 20%) in the etch depth between the outer 10–15 mm at the wafer's edge (where the witness etch features are located) and the rest of the 75 × 60-mm pattern created difficulties in achieving the desired grating etch depth. To overcome this, test samples consisting of four 15 × 60-mm grating stripes having witness etch features adjacent to each stripe were etched and measured. These samples were used to calibrate the RIE process prior to etching the actual 96-mm-diagonal gratings.

The performance of the echelon grating has been modeled using the simplified scalar diffraction theory and rigorous EM diffraction calculations, as shown in Figure 4-9. The EM calculations assume TE polarization and normal incidence (TM polarization results are slightly worse). Results are normalized to

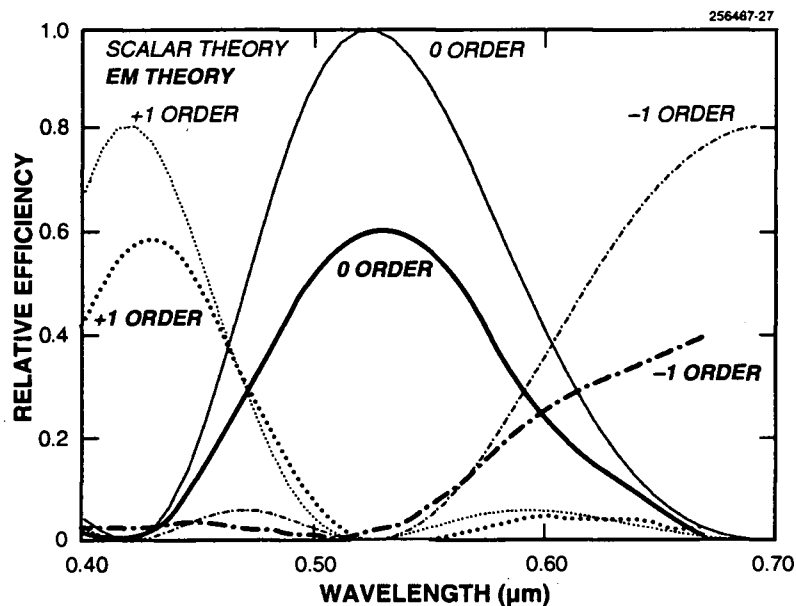
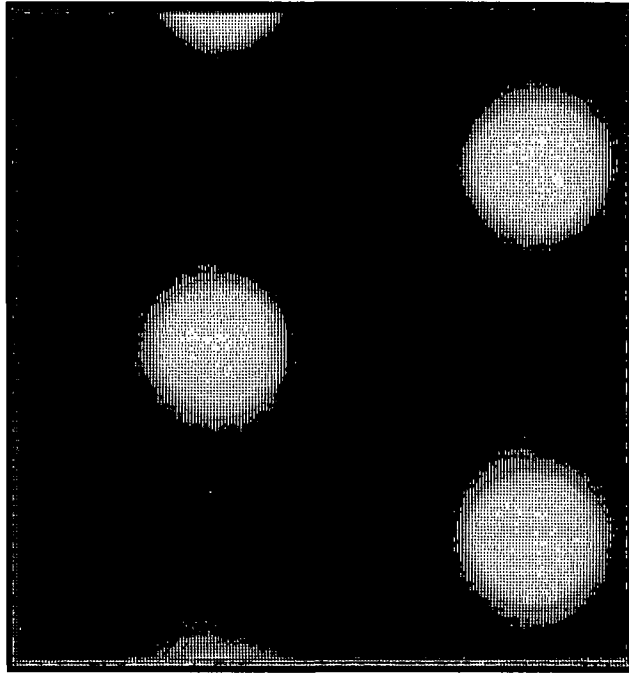
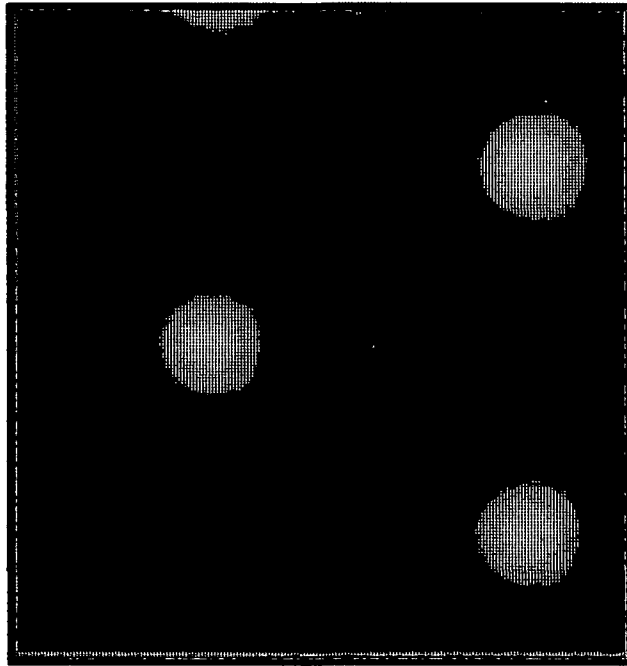


Figure 4-9. Predicted spectral efficiency as function of wavelength for both scalar diffraction theory model and rigorous electromagnetic (EM) calculations. The -1, 0, and +1 order efficiencies are plotted as a function of wavelength.



(a)



(b)

Figure 4-10. Grating performance showing white light transmitted (a) through microlens array and (b) through color separation grating and microlens array.

the total transmitted light. Scalar theory is considered valid when $T \gg \lambda$ and the grating depth is negligible. Because the grating depths for the echelon are not negligible, we expect the 50–60% efficiency predicted by the EM calculations instead of the 80–90% efficiency predicted by the scalar theory. The effects of processing variations on grating performance have also been modeled. The simulations indicate that the etch depth errors must be less than 3% of the minimum step height for the device to function well. Variations in etch depth shift the center frequency to shorter wavelengths if the grating is too shallow and to longer wavelengths if the grating is too deep.

Preliminary evaluation of the color separation optic reveals that the central zero order transmits blue-green light with the red diverted into the -1 order and the blue diverted into the $+1$ order. The grating operation can be observed using a transmission microscope and a microlens array. The microlens array (either 200- μm -diam $\sim f/2$ photoresist lenses or 500- μm -diam $f/4$ Corning SMILE lenses) placed on top of the grating, which is illuminated from below, collects the dispersed light. Color is analyzed via a series of color filters placed over the light source. Results are shown in Figure 4-10(a) for illuminated lenslets without the grating and in Figure 4-10(b) for illuminated lenslets with the grating. Overall, this grating separated light with 45% efficiency compared to the predicted 60%.

M. B. Stern
G. J. Swanson
J. E. Curtin

REFERENCES

1. M. E. Lin, B. Sverdlov, G. L. Zhou, and H. Morkoç, *Appl. Phys. Lett.* **62**, 3479 (1993).
2. T. D. Moustakas, T. Lei, and R. J. Molnar, *Physica B* **185**, 36 (1993).
3. S. Strite, M. E. Lin, and H. Morkoç, *Thin Solid Films* **231**, 197 (1993).
4. M. J. Paisley, Z. Sitar, J. B. Posthill, and R. F. Davis, *J. Vac. Sci. Technol. A* **7**, 701 (1989).
5. R. J. Molnar, T. Lei, and T. D. Moustakas, *Mater. Res. Soc. Proc.* **281**, 765 (1993).
6. T. D. Moustakas and R. J. Molnar, *Mater. Res. Soc. Proc.* **281**, 753 (1993).
7. M. W. Farn, R. E. Knowlden, M. B. Stern, and W. B. Veldkamp, in *NASA Conference Publication 3227, Conference on Binary Optics*, H. J. Cole and W. C. Pittman, eds. (NASA, Washington, D.C., 1993), p. 409.

5. HIGH SPEED ELECTRONICS

5.1 SELF-ALIGNED GaAs MISFETs WITH A LOW-TEMPERATURE-GROWN GaAs GATE INSULATOR

Integrated circuits based on depletion- and enhancement-mode GaAs MESFETs have been widely used for high-speed and low-power applications. However, the gate current of the Schottky contact in a MESFET becomes appreciable at forward biases of several tenths of a volt, imposing severe limits on the maximum drain current, the noise margin, and the flexibility of the bias circuit design. A new type of GaAs MISFET having low-temperature-grown (LTG) GaAs as the gate insulator has a very low gate current at large forward bias and is better suited for these applications. However, the resistivity of the LTG GaAs degrades after a high-temperature anneal because the excess arsenic incorporated in the LTG GaAs can redistribute or escape from the layer during the annealing. A new epitaxial layer structure and fabrication process developed in this work allow the selective doping of the channel outside the gate area by self-aligned n^+ implantation to reduce the channel resistance and the knee voltage of LTG GaAs MISFETs for low-power applications.

All the epitaxial layers in the present structure were grown by molecular beam epitaxy. As shown in Figure 5-1, the epitaxial layers consist of a 2500-Å-thick undoped GaAs buffer, a 2000-Å-thick n -type GaAs channel nominally doped to $8 \times 10^{16} \text{ cm}^{-3}$ with Si, a 200-Å-thick undoped AlAs barrier, an 800-Å-thick undoped LTG GaAs layer grown at 200°C, a 200-Å-thick undoped AlAs barrier, and a 200-Å-thick undoped GaAs cap. All the layers, except for the LTG GaAs, were grown at 600°C. The new feature of this MISFET is the addition of an AlAs barrier layer on top of the LTG GaAs gate insulator. This layer is essential to prevent outdiffusion of the excess As during the implant-activation annealing and thus maintain the high resistivity of the LTG GaAs layer.

To fabricate the MISFETs, a 700-Å-thick W gate was first evaporated and defined by liftoff. The gate length was approximately 1.5 μm . The layers above the conducting channel were chemically etched using the W gate metallization as the etch mask. Then, the source and drain regions were implanted with Si at 30 keV, using the W gate as the mask, to a total dose of $2 \times 10^{13} \text{ cm}^{-2}$. The implanted samples were thermally annealed at 800°C for 10 s. Next, standard Ni/Ge/Au source and drain ohmic contacts were defined by liftoff and alloyed. The spacing between the source and drain ohmic contacts was approximately 7 μm . Finally, the devices were isolated by proton implantation. For comparison, a control sample that was neither implanted nor annealed was also processed on the same material in parallel with the self-aligned MISFET.

The sheet resistance of the conducting channel outside the gate area was 1700 Ω/square without Si implantation, and was reduced by the implant to 620 Ω/square . The contact resistance was also improved from $6.6 \times 10^{-6} \Omega \text{ cm}^2$ for the control sample to $1.1 \times 10^{-6} \Omega \text{ cm}^2$ for the implanted sample. The drain-source current (I_{ds}) vs drain-source voltage (V_{ds}) characteristics of the MISFETs are shown in Figure 5-2. The maximum drain current obtainable was 65 mA/mm ($V_{gs} = +2 \text{ V}$) for the control sample and 160 mA/mm ($V_{gs} = +4 \text{ V}$) for the implanted sample. The maximum transconductance g_m also increased from approximately 20 mS/mm for the control to 35 mS/mm for the implanted sample. Notice that even at 6 V of forward gate bias, there is no sign of gate conduction. The forward-bias gate current

of the self-aligned MISFET is slightly higher than that of the control MISFET as a result of the high-temperature treatment. At a forward-bias gate current of 10 nA per μm^2 gate area, which is acceptable for many low-power applications, the corresponding positive voltages on the gate are 1.83 and 1.56 V for MISFETs on the control and implanted samples, respectively. Therefore, for a supply voltage of 1.5 V or lower, which is common for low-power circuits, the gate of the MISFET can be connected directly to the power supply, greatly simplifying the design of the bias and the coupling circuits. The reverse gate-breakdown voltage (also defined at 10 nA per μm^2 gate area) is approximately 20 V for both samples and appears not sensitive to the annealing.

RF measurements were performed using microwave on-wafer probes. The unity-current-gain frequency f_T , derived from measured small-signal scattering parameters, is 2.2 GHz for the control sample and 5.7 GHz for the implanted sample. The drain bias was kept at 2 V, and gate biases, chosen for a high g_m , were -0.5 and 0 V, respectively. The corresponding values of the maximum frequency of oscillation f_{max} are 1.6 and 2.9 GHz, respectively. The relatively low f_{max} values are probably caused by the high resistance of the thin W gate and can be improved by increasing the metal thickness or using different refractory gate metal having a lower resistivity.

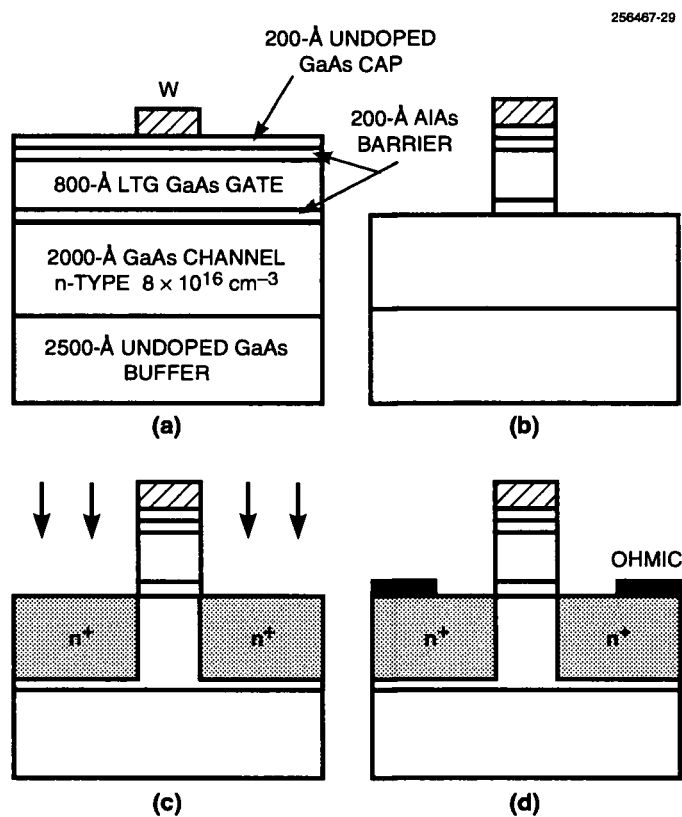
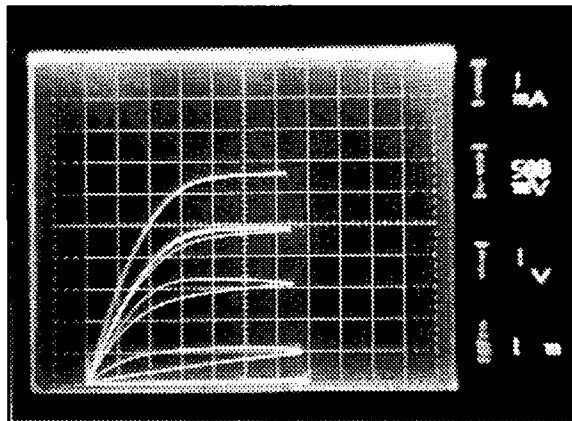
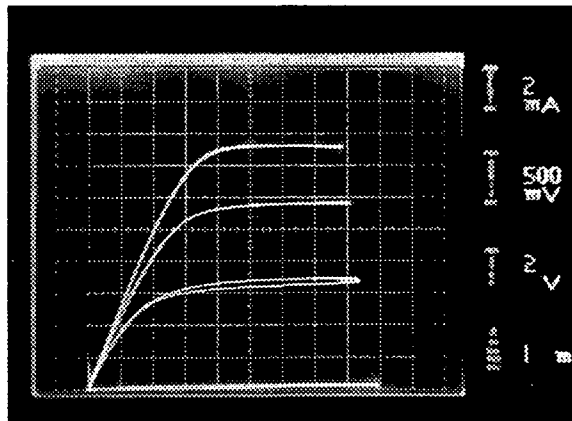


Figure 5-1. Layer structures and process steps for self-aligned LTG GaAs MISFET: (a) Deposition of W gate, (b) etching off LTG GaAs and AlAs layers, (c) self-aligned n^+ implantation, and (d) deposition and alloying of ohmic contacts.



(a)



(b)

Figure 5-2. I_{ds} vs V_{ds} characteristics of MISFETs with 100- μm -wide gate width. (a) Control MISFET; the vertical scale is 1 mA/div and V_{gs} is +2 V for the top curve with 1-V steps. (b) Self-aligned MISFET with 30-keV implant; the vertical scale is 2 mA/div and V_{gs} is +4 V for the top curve with 2-V steps. The horizontal scale is 500 mV/div for all the I-V curves.

The improvement of the self-aligned LTG GaAs MISFET resulting from the n^+ implantation is clearly shown. The speed of the MISFET can be easily increased by reducing the gate length and the thickness of the LTG GaAs insulator and optimizing the implant and annealing schedules. The fabrication process is simple and is standard for GaAs integrated circuits. Because there is no gate recess, the threshold voltage is determined mainly by the epitaxial growth, and good device uniformity can be expected.

C. L. Chen	B. F. Gramstorff
L. J. Mahoney	K. M. Molvar
K. B. Nichols	R. A. Murphy
M. J. Manfra	E. R. Brown

6. MICROELECTRONICS

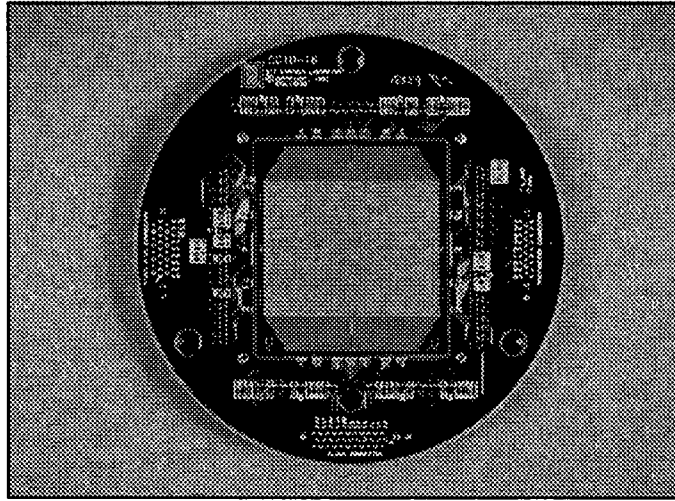
6.1 PACKAGING OF A 1960×2560 -PIXEL CHARGE-COUPLED DEVICE IMAGER

A large frame-transfer CCD imager occupying an entire 100-mm silicon wafer was described recently [1]. This device has a die size of 67×74 mm and is the largest image sensor ever made. No integrated-circuit package exists for a device of this size, and therefore we had to develop a custom package. In this report we describe the package structure and the various novel features that make it more attractive than conventional packaging.

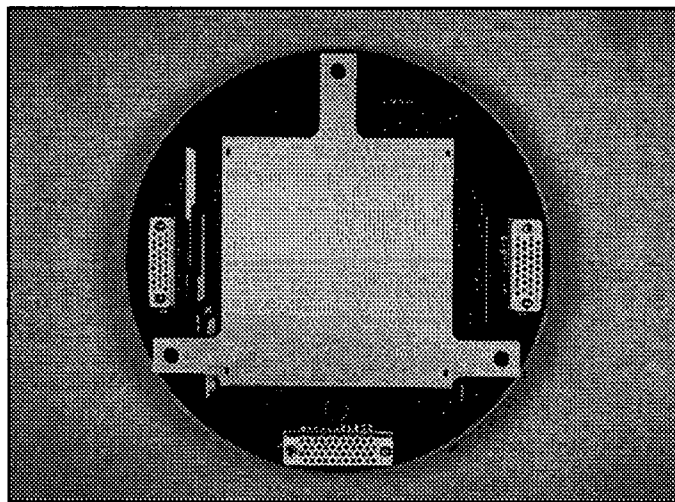
For our smaller CCD imagers, we use Kovar packages with pins arranged around the periphery. The Kovar provides reasonable thermal conductivity for efficient cooling of the device, and with the pins confined to the periphery a cold finger can make maximum area contact to the back of the package. The pins are typically spaced uniformly on 0.100-in. centers, but the CCD pads often cannot be designed to this spacing, as in the case of a three-side-abutable imager [2] where they are clustered along one edge of the die. This forces us to mount the CCD on an alumina (Al_2O_3) plate, which is then mounted in the package well. The alumina has thin-film metallization traces that bring the signals from the package leads to the CCD pads so that wire-bond lengths can be kept short. The alumina plate is not an optimal material in terms of matching to the coefficient of thermal expansion (CTE) of silicon, although this has not been a problem for smaller devices.

We have developed a novel package for the 1960×2560 -pixel imager, and Figure 6-1 shows photographs of the front and back of a packaged device. The package consists of two parts, a metal plate upon which the device is mounted and a multilayer printed-circuit board (PCB) that surrounds the device and is attached to the metal plate. The diameter of the card is 152.4 mm (6.000 in.) and is fabricated from G10 fiberglass in ten layers (five signal and five ground). We are free to select a metal that is a good CTE match to silicon so stresses to the device are minimized, and that can be readily machined to a flatness specification of $\pm 10 \mu\text{m}$. Thermal conductivity is not a major concern, as the thermal resistance of a plate made from any of the candidate materials together with the maximum thermal load on the device would lead to less than 1°C temperature difference between the CCD and the back of the plate. We could not specify quantitatively the degree of CTE match, and indeed we have found no device failures attributable to mechanical stresses in 1024×1024 -pixel devices (roughly one-fourth the area of this device) mounted with epoxy on alumina substrates and cooled to -130°C . Nevertheless, given the larger device area we felt that a CTE match at least as close as that of alumina was desirable.

Table 6-1 compares the CTE of silicon to some of the candidate materials as well as alumina. Aluminum, and indeed most common metals, have a CTE poorly matched to silicon. Invar 36 is very close to silicon but has the fabrication disadvantage that it must be heat treated after machining to maintain the low CTE. Kovar has a better CTE than alumina but might not maintain the required flatness over the temperature range because it is rolled. We chose molybdenum because its CTE is better matched to silicon than that of alumina, it can be readily machined, and it should have isotropic expansion because of its pressed, sintered condition. Molybdenum does not require any surface treatment, unlike Invar 36 and Kovar which must be plated because of their iron content.



(a)



(b)

Figure 6-1. Photographs of (a) front and (b) back of packaged large-area charge-coupled device imager.

The PCB has a number of attractive features not possible with a conventional Kovar package. In our structure the signals are brought onto the board via three standard, multipin connectors (Positronics). This approach effectively eliminates the difficult step of mounting a large multipin package in a conventional socket, which requires careful alignment of the pins to the socket and large pressure to seat the package. The popular “zero-insertion pressure,” or ZIP sockets, are not nearly large enough for a package that

TABLE 6-1**Comparison Between Coefficient of Thermal Expansion of Silicon and Other Materials**

Material	Thermal Expansion Coefficient (ppm/°C)
Silicon	2.0
Alumina (Al ₂ O ₃)	6.7
Aluminum	23
Invar 36	1.6
Kovar	5.2
Molybdenum	4.9

would accommodate this chip. The CCD pads are wire bonded directly to gold-plated traces on the board, and this reduces the number of wire bonds by 2× compared to the case of the chip/alumina-board/Kovar package combination.

Another attractive feature of the PCB is the opportunity to include circuitry and to isolate the digital clock signals from the low-noise analog lines. Separate digital and analog ground planes are used, and the dc lines that are critical to low-noise performance are bypassed with capacitors. Low-noise junction field-effect transistor source followers are used to buffer all output video lines. Because of the multilayer feature, many of the CCD functions that require the same driving voltage (e.g., reset gates) could be wired in common to reduce the number of input/output leads. Each clock line is protected from electrostatic discharge (ESD) by a circuit, illustrated in Figure 6-2 [3]. The 0.1-μF capacitors represent about 3 orders of magnitude more capacitance than a human body, so an ESD voltage will be attenuated by that amount. The 1-MΩ resistors bleed away the charge with a time constant of 0.1 s. When the device is powered up, the capacitor on the left leg will charge up close to the most positive voltage of the clocks, while the capacitor on the right will similarly charge to nearly the most negative level. Once charged, the capacitors will stay at their levels because of the long discharge time and because normally at least one of the clock phases is driven to one of the extreme voltages at any given time. The clock lines are then coupled to each other only through the small reverse-bias capacitance of the diodes.

Several devices have been mounted in this package and cycled repeatedly to -70°C with no adverse effects.

B. E. Burke J. W. Caunt
P. J. Daniels K. A. Percival

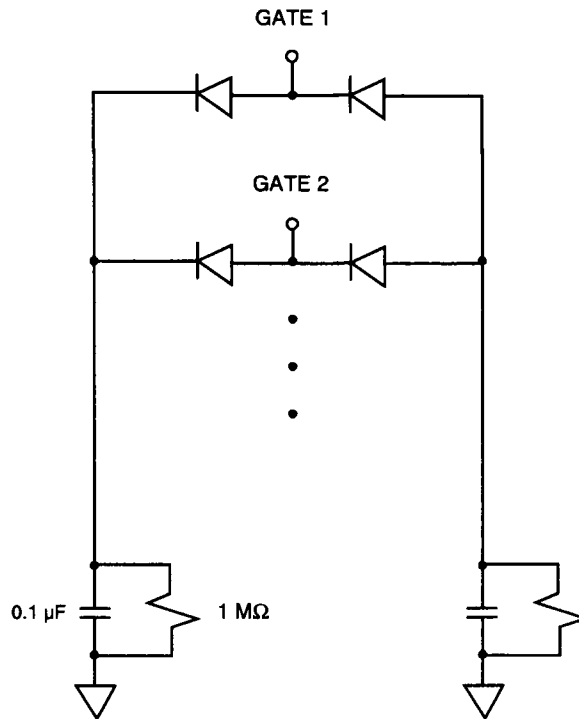


Figure 6-2. Schematic of electrostatic discharge circuit that protects each clock line.

REFERENCES

1. Solid State Research Report, Lincoln Laboratory, MIT, 1993:4, p. 39.
2. B. E. Burke, R. W. Mountain, D. C. Harrison, M. W. Bautz, J. P. Doty, G. R. Ricker, and P. J. Daniels, *IEEE Trans. Electron Devices* **38**, 1069 (1991).
3. J. Doty, Center for Space Research, MIT, private communication.

7. ANALOG DEVICE TECHNOLOGY

7.1 LINCOLN/HUGHES COMPRESSIVE RECEIVER DEMONSTRATION WITH 24-ns BONDED-WAFER $\text{YBa}_2\text{Cu}_3\text{O}_{7-\delta}$ CHIRP FILTERS

The ability to detect many simultaneous signals with 100% time coverage gives the compressive receiver a distinct advantage over conventional electronic-warfare (EW) receivers, such as superheterodyne, instantaneous frequency measurement, or crystal video receivers [1]. The compressive receiver accomplishes this simultaneous signal detection through an analog implementation of the chirp transform process using dispersive-delay-line chirp filters. High-temperature superconductive (HTS) chirp filters offer the opportunity to enhance the instantaneous bandwidth coverage of modern compressive receivers. The multigigahertz bandwidth of HTS chirp filters is unavailable from present surface acoustic wave (SAW) technology. Notably, SAW chirp filters are limited to less than a 1-GHz bandwidth.

Lincoln Laboratory recently demonstrated a 3-GHz bandwidth compressive receiver based on 12-ns HTS chirp filters [2], which has now been space qualified for flight on the Navy's second High-Temperature Superconductor Space Experiment [3]. This receiver had only a simple frequency cueing capability; a more complete demonstration would also report pulse width, amplitude, and time of arrival, as is done in a stand-alone EW receiver. Hughes Aircraft Company has recently completed a 1-GHz-bandwidth stand-alone compressive receiver based on SAW chirp filters. Although the analog and digital electronics in the Hughes receiver are matched to the narrower bandwidth of the SAW filters, we report here that the receiver has demonstrated full functionality and 2-GHz bandwidth with an HTS chirp filter replacing the SAW filters. This has doubled the instantaneous bandwidth coverage of the Hughes EW receiver. For this demonstration an HTS chirp filter with 24 ns of dispersive delay was developed, doubling the frequency resolution attainable with the earlier 12-ns HTS filter.

Superconductive chirp filters were initially implemented in niobium at 4.2 K [4], but the very low cryogenic temperature prevented insertion into systems. The rapid progress that has been made in microwave applications of high-temperature superconductors has produced an opportunity to take advantage of the more feasible liquid-nitrogen temperatures required by the HTS materials [5]. An important technical challenge for HTS chirp filters is to increase the length of the tapped delay lines constituting the filter. Longer delay will produce more signal processing gain in the filter and result in improved frequency resolution in a compressive receiver. The HTS chirp filters are based on a stripline configuration that uses two symmetrically placed ground planes on opposite sides of a pair of wafers. The packing density of the delay lines, and therefore the total chirp filter length, is directly proportional to the thickness of the two wafers. As the wafer thickness is reduced, a support wafer is required to prevent the thin wafer from breaking.

Figure 7-1 diagrams the technique used to bond a thin LaAlO_3 wafer to a thick LaAlO_3 support wafer, and shows a photograph of a 24-ns $\text{YBa}_2\text{Cu}_3\text{O}_{7-\delta}$ (YBCO) chirp filter fabricated using the technique. The wafer-bonding process begins with a 10-mil-thick LaAlO_3 upper wafer with a sputtered layer of Ti/Au on the bottom surface, a 20-mil-thick LaAlO_3 base wafer, and gold foil between the two wafers. The wafers and the gold foil must be kept very clean throughout the entire bonding process. The wafers are forced together against the gold foil in a press. The bonded-wafer pair is then placed in a standard gas-pocket heater and YBCO is grown in a cylindrical magnetron sputtering system on the top surface of the thin wafer [6]. Standard

YBCO patterning techniques can be used following the YBCO growth [7]. The edges of the gold foil are used to make contact to the ground plane on the bottom surface of the thin wafer. A second bonded-wafer pair is required for the upper ground plane of the stripline configuration.

The success of the bonded-wafer technique is validated by the performance of the 24-ns YBCO chirp filter, illustrated in Figures 7-2 and 7-3. The measured group delay vs frequency in the downchirp mode is plotted in Figure 7-2 for an operating temperature of 77 K. The linearity of the group delay vs frequency illustrates the correct chirp response of the filter. The time-domain reflectometry response of the same chirp filter is shown in Figure 7-3(a). This is essentially a low-frequency measurement, below the cut-off frequency of the Klopfenstein impedance tapers, and is taken on one of the two transmission lines that constitute the chirp filter. From left to right, the response shows reflections from a 50-Ω input connector, an inductive discontinuity from the connector to stripline transition, the taper from a 50-Ω narrow linewidth to a 32-Ω wide linewidth, a constant 32-Ω linewidth, a second taper from a 32-Ω linewidth to a 50-Ω linewidth, another inductive discontinuity, and back to a 50-Ω output connector. The time-domain downchirp response to a step function is shown in Figure 7-3(b). This measurement is performed on the input and output ports of the chirp filter that produce a downchirp. The frequency components of the step function input that are above the cut-off frequency of the impedance tapers appear at the output port. The response appears for each of the 96 backward-wave couplers. The Hamming weighting of the couplers is evident.

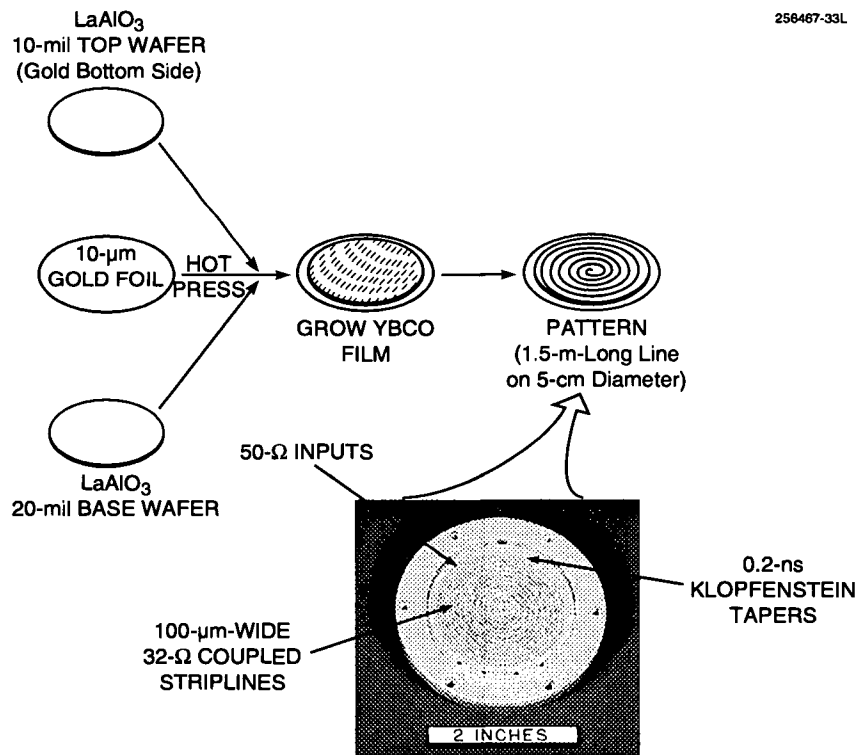


Figure 7-1. Illustration of LaAlO₃ wafer bonding technique used to fabricate 24-ns stripline YBCO chirp filters. The 24-ns filter is shown as an inset.

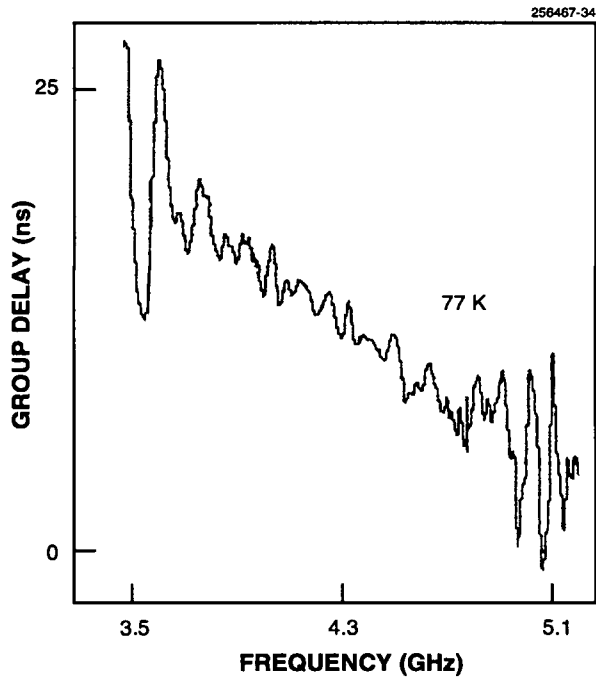


Figure 7-2. Group delay vs frequency characteristic measured using downchirp ports of 24-ns YBCO chirp filter.

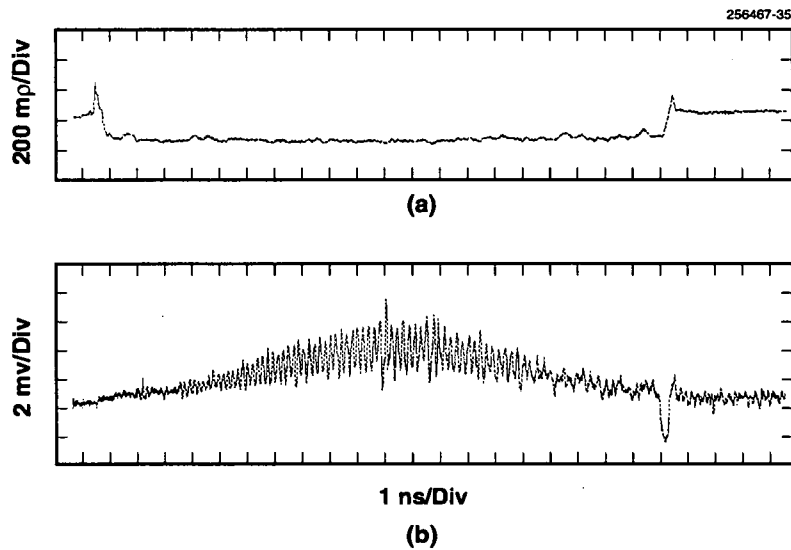


Figure 7-3. Time-domain response of 24-ns YBCO chirp filter: (a) Time-domain reflectometry measured at 77 K for one of the two YBCO striplines that constitute the 24-ns filter and (b) low-frequency time-domain response to a step function measured at 77 K.

The configuration chosen to combine the Hughes EW receiver with the Lincoln HTS chirp filter front end is shown in Figure 7-4. The Hughes compressive receiver produces pulse-descriptor words for multiple emitters. The descriptor words contain the emitter frequency, amplitude, pulse width, and time of arrival (TOA). In Figure 7-4 the attenuated signal between 9.8 and 11.8 GHz is switched with a pulse generator to simulate input from pulsed emitters. The ramp generator and voltage-controlled oscillator (VCO) combination functions as a chirp generator to produce an upchirp, which is mixed with the pulsed input. Pulse generator 2 switches off the input during the time that the VCO is sweeping down in frequency (downchirp blanking). The final local oscillator and mixer combination downconverts the chirp transform output to the intermediate frequency of the Hughes receiver. A scan sync pulse synchronizes the analysis window of the Hughes receiver and the chirp transform front end.

The results of the initial Lincoln/Hughes demonstration are presented in Table 7-1. The Hughes receiver with the 2-GHz-bandwidth HTS chirp filter front end demonstrated full functionality. The frequency vs time characteristic of the HTS chirp filter is significantly better than the characteristic of the VCO-based chirp generator. The single-tone dynamic range is therefore limited by the error sidelobes of the chirp generator and

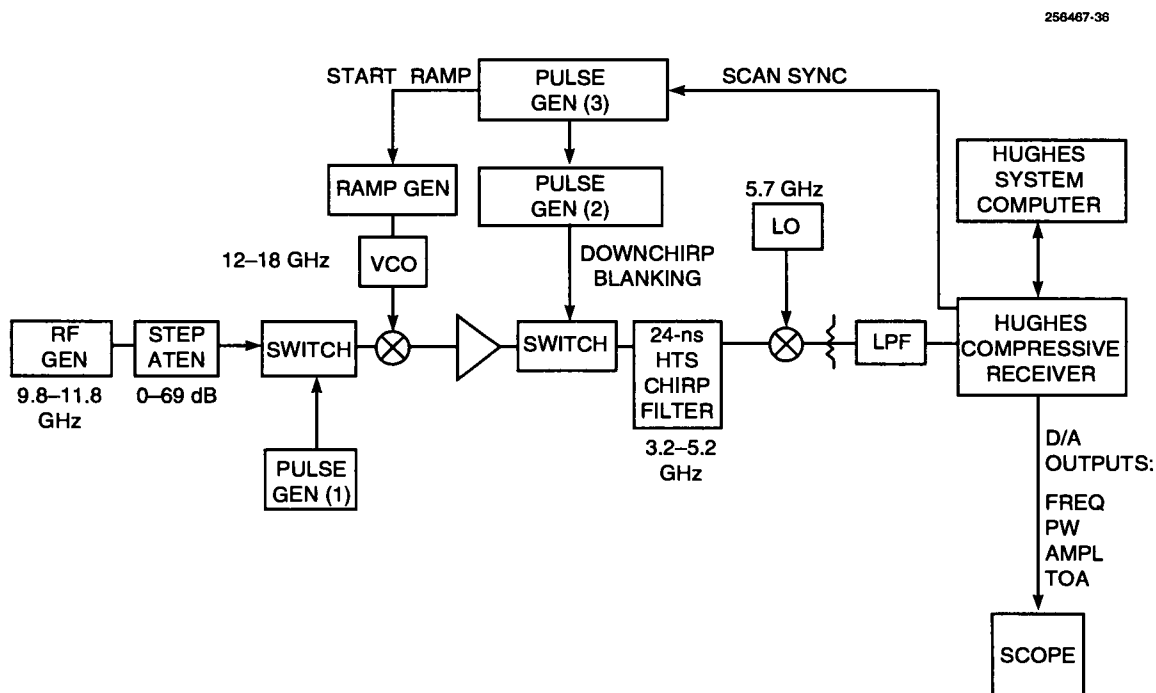


Figure 7-4. System block diagram for Lincoln/Hughes demonstration. Interfaces to the Hughes receiver and computer system are indicated.

TABLE 7-1**Summary of Lincoln/Hughes Compressive Receiver Demonstration**

Parameter	Measured Performance
RF input bandwidth	2 GHz
RF frequency resolution	2 GHz/24 Cells = 83 MHz
Time of arrival and pulse-width resolution	200 ns
Dynamic range, single tone	30 dB*
Simultaneous signal detection	Up to 3
Short-pulse (100–400 ns) probability of intercept	50%
Long-pulse (> 400 ns) probability of intercept	100%
Amplitude resolution	1dB
* > 50 dB with manual threshold adjustment.	

not the HTS chirp filter itself. These error sidelobe levels act as spurious signals, limiting the single-tone dynamic range with a fixed threshold to 30 dB. The receiver is limited to 200-ns TOA resolution and only 50% probability of intercept for short (100-400 ns) pulses because the receiver was designed to operate with 200-ns-long SAW chirp filters and has a 200-ns analysis window. The frequency resolution is limited by the 1-GHz frequency cell counter, which counts only 24 times in 24 ns, producing a resolution of 2 GHz/24 cells = 83 MHz. A faster cell counter would not improve the resolution since the receiver's 1-GHz log amplifiers elongate the 2-GHz-bandwidth compressed pulses generated by the HTS chirp filter. No more than three simultaneous signals can be detected because the Hughes receiver requires that detected compressed pulses be at least 8 ns apart, and the HTS chirp filter is 24 ns long.

W. G. Lyons	M. M. Seaver
D. Barry*	D. R. Arsenault
R. Guadagnolo*	R. L. Slattery
P. G. Murphy	D. J. Baker
R. R. Boisvert	E. M. Macedo
A. C. Anderson	G. L. Fitch

*Author not at Lincoln Laboratory.

REFERENCES

1. K. D. Breuer, J. S. Levy, and H. C. Paczkowski, *Microwave J.* **32** (10), 81 (1989).
2. W. G. Lyons, M. M. Seaver, D. R. Arsenault, R. R. Boisvert, and T. C. L. G. Sollner, *Microw. Opt. Technol. Lett.* **6**, 728 (1993); **7**, 875 (1994).
3. T. C. L. G. Sollner, W. G. Lyons, D. R. Arsenault, A. C. Anderson, M. M. Seaver, R. R. Boisvert, and R. L. Slattery, to be published in *IEEE Trans. Appl. Superconduct.* **5**(2) (1995).
4. R. S. Withers and R. W. Ralston, *Proc. IEEE* **77**, 1247 (1989).
5. N. Newman and W. G. Lyons, *J. Superconduct.* **6**, 119 (1993).
6. Solid State Research Report, Lincoln Laboratory, MIT, 1993:2, p. 31.
7. W. G. Lyons, R. S. Withers, J. M. Hamm, A. C. Anderson, D. E. Oates, P. M. Mankiewich, M. L. O'Malley, R. R. Bonetti, A. E. Williams, and N. Newman, in *Superconductivity and Its Applications*, Y. H. Kao, A. E. Kaloyeros, and H. S. Kwok, eds. (American Institute of Physics, New York, 1992), Vol. 251, p. 639.

REPORT DOCUMENTATION PAGE

Form Approved
OMB No. 0704-0188

Public reporting burden for this collection of information is estimated to average 1 hour per response, including the time for reviewing instructions, searching existing data sources, gathering and maintaining the data needed, and completing and reviewing the collection of information. Send comments regarding this burden estimate or any other aspect of this collection of information, including suggestions for reducing this burden, to Washington Headquarters Services, Directorate for Information Operations and Reports, 1215 Jefferson Davis Highway, Suite 1204, Arlington, VA 22202-4302, and to the Office of Management and Budget, Paperwork Reduction Project (0704-0188), Washington, DC 20503.

1. AGENCY USE ONLY (Leave blank)	2. REPORT DATE 15 February 1995	3. REPORT TYPE AND DATES COVERED Quarterly Technical Report, 1 November 1994-31 January 1995	
4. TITLE AND SUBTITLE Solid State Research		5. FUNDING NUMBERS C — F19628-95-C-0002 PE — 63250F PR — 221	
6. AUTHOR(S) David C. Shaver		8. PERFORMING ORGANIZATION REPORT NUMBER 1995:1	
7. PERFORMING ORGANIZATION NAME(S) AND ADDRESS(ES) Lincoln Laboratory, MIT 244 Wood Street Lexington, MA 02173-9108		10. SPONSORING/MONITORING AGENCY REPORT NUMBER ESC-TR-95-023	
9. SPONSORING/MONITORING AGENCY NAME(S) AND ADDRESS(ES) HQ Air Force Materiel Command AFMC/STSC Wright-Patterson AFB, OH 45433-5001		11. SUPPLEMENTARY NOTES None	
12a. DISTRIBUTION/AVAILABILITY STATEMENT Approved for public release; distribution is unlimited.		12b. DISTRIBUTION CODE	
13. ABSTRACT (Maximum 200 words) <p style="text-align: center;">This report covers in detail the research work of the Solid State Division at Lincoln Laboratory for the period 1 November 1994-31 January 1995. The topics covered are Electrooptical Devices, Quantum Electronics, Materials Research, Submicrometer Technology, High Speed Electronics, Microelectronics, and Analog Device Technology. Funding is provided primarily by the Air Force, with additional support provided by the Army, ARPA, Navy, BMDO, NASA, and NIST.</p>			
14. SUBJECT TERMS electrooptical devices high-speed electronics monolithic optoelectronic transistors field-effect transistors quantum electronics microelectronics lasers charge-coupled device imagers materials research analog device technology epitaxial growth superconductive filters submicrometer technology smart-pixel arrays binary optics			15. NUMBER OF PAGES 68
17. SECURITY CLASSIFICATION OF REPORT Unclassified			16. PRICE CODE
18. SECURITY CLASSIFICATION OF THIS PAGE Same as Report	19. SECURITY CLASSIFICATION OF ABSTRACT Same as Report	20. LIMITATION OF ABSTRACT Same as Report	